

IDENTIFICATION OF FAINT *CHANDRA* X-RAY SOURCES IN THE CORE-COLLAPSED GLOBULAR CLUSTER NGC 6752

PHYLLIS M. LUGGER,¹ HALDAN N. COHN,² ADRIENNE M. COOL,³ CRAIG O. HEINKE,⁴ AND JAY ANDERSON⁵

¹*Department of Astronomy, Indiana University, 727 E. Third St., Bloomington, IN 47405, USA; lugger@indiana.edu*

²*Department of Astronomy, Indiana University, 727 E. Third St., Bloomington, IN 47405, USA; cohn@indiana.edu*

³*Department of Physics and Astronomy, San Francisco State University, 1600 Holloway Avenue, San Francisco, CA 94132, USA; cool@sfsu.edu*

⁴*Department of Physics, University of Alberta, Edmonton, AB T6G 2G7, Canada; heinke@ualberta.ca*

⁵*Space Telescope Science Institute, 3700 San Martin Dr., Baltimore, MD 21218, USA; jayander@stsci.edu*

(Published in the *Astrophysical Journal*, 2017, 241, 53)

ABSTRACT

We have searched for optical identifications for 39 *Chandra* X-ray sources that lie within the $1\frac{1}{9}$ half-mass radius of the nearby ($d = 4.0$ kpc), core-collapsed globular cluster, NGC 6752, using deep *Hubble Space Telescope* ACS/WFC imaging in B_{435} , R_{625} , and $H\alpha$. Photometry of these images allows us to classify candidate counterparts based primarily on color-magnitude and color-color diagram location. The color-color diagram is particularly useful for quantifying the $H\alpha$ -line equivalent width. In addition to recovering 11 previously detected optical counterparts, we propose 20 new optical IDs. In total, there are 16 likely or less certain cataclysmic variables (CVs), nine likely or less certain chromospherically active binaries, three galaxies, and three active galactic nuclei (AGNs). The latter three sources, which had been identified as likely CVs by previous investigations, now appear to be extragalactic objects based on their proper motions. As we previously found for NGC 6397, the CV candidates in NGC 6752 fall into a bright group that is centrally concentrated relative to the turnoff-mass stars and a faint group that has a spatial distribution that is more similar to that of the turnoff-mass stars. This is consistent with an evolutionary scenario in which CVs are produced by dynamical interactions near the cluster center and diffuse to larger radius orbits as they age.

Keywords: globular clusters: individual (NGC 6752) — X-rays: binaries — novae, cataclysmic variables

1. INTRODUCTION

Joint *Chandra X-ray Observatory* and *Hubble Space Telescope* (*HST*) observations of globular clusters have revealed large populations of faint X-ray sources ($L_X \lesssim 10^{33.5} \text{ erg s}^{-1}$) which include quiescent low-mass X-ray binaries (qLMXBs), cataclysmic variables (CVs), chromospherically active binaries (ABs), and millisecond pulsars (MSPs) (Verbunt & Lewin 2006; Heinke 2010). These populations range in size from tens to hundreds of objects per cluster. The presence of these objects is closely related to the cluster dynamics, as demonstrated by Pooley et al. (2003), who found the existence of a strong correlation between the source population size and the encounter rate in the cluster core, $\Gamma \propto \rho_0^2 r_c^3 v_0^{-1}$, where ρ_0 is the central density, r_c is the core radius, and v_0 is the central velocity dispersion. Pooley & Hut (2006) subsequently found evidence that the majority of CVs in dense globular clusters were produced dynamically. Clusters that undergo core collapse pass through phases of extremely high central density and are thus expected to undergo repeated bursts of close binary production in their cores. It is therefore of great interest to examine the faint X-ray source populations in core-collapsed clusters.

In a previous study, we carried out a deep *HST* ACS/WFC imaging study of the nearest core-collapsed globular cluster NGC 6397 in the filters F435W (B_{435}), F625W (R_{625}), and F658N ($H\alpha$), in which we identified optical counterparts to 69 of the 79 *Chandra* sources that lie within the half-mass radius (Cohn et al. 2010). A striking finding of this study was that there is a bimodal distribution of CVs, consisting of a brighter group of six for which the optical emission is dominated by contributions from the secondary and the accretion disk, and a fainter group of seven for which the white dwarf dominates the optical emission. The brighter CVs are much more concentrated towards the cluster center than the fainter CVs. We speculated that this may be the result of dynamical evolution in which CVs are formed in and near the cluster core and subsequently migrate to larger distances from the cluster center as they age and become fainter. The faintest CVs that we identified in our study of NGC 6397 have absolute magnitudes around $M_R \sim 11.2$ that likely put them near the minimum of the CV period distribution found in the Sloan Digital Sky Survey (Gänsicke et al. 2009). Cool et al. (2013) used *HST* imaging to search for optical counterparts to *Chandra* sources in the massive globular cluster ω Cen. They reported finding 27 candidate CVs, of which 14 lie in the magnitude range $M_R \sim 10.4 - 12.6$. Thus, faint CV populations that likely extend to the minimum of the CV period distribution are known to exist in two globular clusters.

To extend the search for faint CV populations, we have investigated NGC 6752, the second closest core-collapsed cluster at a distance of 4.0 kpc (Harris 1996). The puzzling dynamical status of NGC 6752 has been addressed in

a number of studies. Djorgovski & King (1986) classified the cluster as core-collapsed based on its ground-based B -band surface-brightness profile, which shows a power-law region outside of a resolved core. In Lugger et al. (1995), we reexamined the profile using ground-based U -band data, which is less affected by bright giants, and found that it could be fitted by either a modified power law (power-law + core) or a standard King model, with the former providing a somewhat better fit than the latter. We nevertheless advanced the conservative interpretation that NGC 6752 is not required to be in a post-collapse state. Ferraro et al. (2003) used a combination of *HST* WFPC2 and ground-based images to construct surface-brightness and surface-density profiles, finding that these are best fitted by a double King model, viz. one King model to describe the inner profile and another one to describe the outer profile. They took this as evidence that NGC 6752 is experiencing a post-core-collapse bounce. Most recently, Thomson et al. (2012) obtained surface-density profiles from *HST* ACS imaging, again finding that the profile is not well described by a single King model. They present a double-King-model fit and conclude that the cluster is either in a core-collapsed or post-core-collapse state. They note that the double King model is purely phenomenological, without a physical basis. Based on this previous work, we have undertaken a reexamination of the surface-density profile of NGC 6752 in the present study.

The X-ray source population of NGC 6752 has been previously studied by Pooley et al. (2002), Kaluzny & Thompson (2009), and Thomson et al. (2012). Pooley et al. (2002) identified a total of 19 *Chandra* sources within the $115''$ half-mass radius of the cluster to a limiting X-ray luminosity of $L_X \sim 10^{30} \text{ erg s}^{-1}$. They proposed 12 optical identifications based on archival *HST* WFPC2 imaging and one radio identification. They found that 10 of the sources are likely to be CVs, one to three are likely to be ABs, and one or two are possible background objects. Kaluzny & Thompson (2009) identified a periodic variable that they suggested as the optical counterpart to the Pooley et al. (2002) source CX19. Thomson et al. (2012) reanalyzed the identifications of the Pooley et al. (2002) sources using multi-wavelength imaging (FUV to I -band) from the *HST* STIS, ACS, and WFC3. They identified dwarf nova outbursts from two previously identified CVs, suggested optical counterparts to CX8 and CX12 (and an alternate optical counterpart to CX16), and failed to confirm suggested counterparts to CX11 (Pooley et al. 2002) and CX19 (Kaluzny & Thompson 2009).

The *Chandra* study by Pooley et al. (2002) is based on 29 ks of the total of 67 ks of ACIS exposure that is available for this cluster. Forestell et al. (2014) have analyzed the complete dataset, detecting 39 sources within the half-mass radius, to a limiting luminosity of $L_X \approx 5 \times 10^{29} \text{ erg s}^{-1}$. In order to search for counterparts of this deeper set of *Chan-*

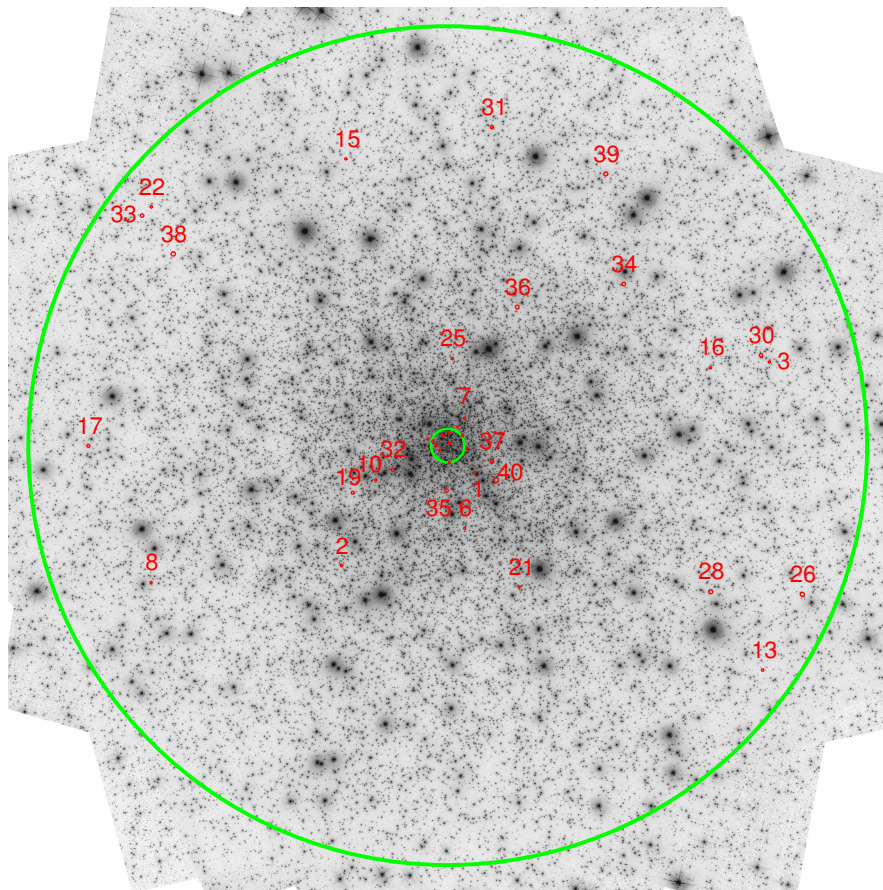


Figure 1. Drizzle-combined *HST* ACS/WFC $H\alpha$ mosaic of NGC 6752 with search regions for *Chandra* sources within the half-mass radius. North is up and east is to the left. The inner green circle represents the core radius of $4''.6$ and the outer green circle represents the half-mass radius of $1''.9$. Source labels are omitted near the core for clarity. There are a total of 39 sources detected within the half-mass radius. The search region radius is defined as the maximum of 2.5 times the formal error circle radius and $0''.3$.

dra sources, we have made use of the ACS/WFC imaging database that is also being used to search for helium-core white dwarfs in NGC 6752 (Hernandez et al. 2013), results of which will be reported elsewhere.

In the following sections, we describe the *Chandra* and *HST* datasets that we use in this study, the method that we use to analyze the *HST* dataset to find optical counterparts to the *Chandra* sources, the set of counterparts that results from this analysis, the optical variability of the counterparts, and the spatial distribution of the stars and X-ray sources in NGC 6752.

2. DATA

The *Chandra* imaging used in this study is the combination of Observation IDs 948 (PI: Lewin) and 6612 (PI: Heinke), which were carried out with the ACIS-S instrument. The exposure times for these datasets are 29 ks and 38 ks respectively. The processing of these data is described in detail by Forestell et al. (2014). Source detections were made with the `wavdetect` and `pwdetect` software utilities. This

resulted in a catalog of 39 sources within the half-mass radius of NGC 6752, extending the previous catalog numbering by Pooley et al. (2002) in order of decreasing source brightness.¹ We restrict the present study to the analysis of these 39 sources.

The optical imaging used in this study is the *HST* GO-12254 dataset (PI: Cool), which provides deep, highly dithered ACS/WFC imaging of the half-mass radius region of NGC 6752 in B_{435} , R_{625} , and $H\alpha$. The dither strategy was designed to recover the full angular resolution of the *HST*, which is advantageous for performing photometry in the very crowded central regions of NGC 6752. The images were obtained over six 2-orbit visits, spread over 180 d, in order to sample the stellar point-spread function (PSF) at a range of roll angles. When combined by a drizzling technique, the resulting mosaic images are free of diffraction

¹ Note that CX12 from Pooley et al. (2002) is divided into three sources in this new catalog, viz. CX20, CX23, and CX24.

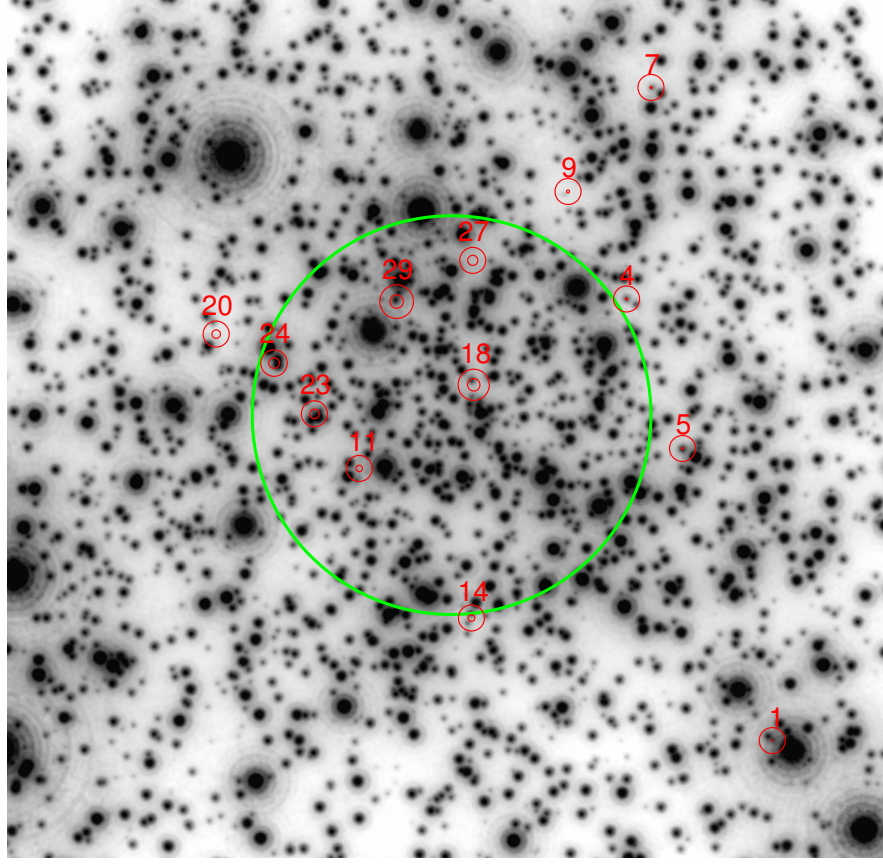


Figure 2. The core-radius region of the drizzle-combined $H\alpha$ mosaic of NGC 6752 with error circles and search regions for *Chandra* sources. The green circle represents the core radius of $4''.6$.

spikes and similar PSF artifacts. The dataset consists of 6 short B_{435} (10 s), 12 long B_{435} (380 s), 6 short R_{625} (10 s), 12 long R_{625} (360 s), and 24 $H\alpha$ (12 each of 724 s and 820 s) exposures. The short exposures were designed to provide accurate photometry for stars above the main-sequence turnoff (MSTO). With the large number of $H\alpha$ frames, the PSF sampling is particularly complete for this band.

3. ANALYSIS METHOD

3.1. Photometry

The *HST* data were analyzed using software based on the program developed for the ACS Globular Cluster Treasury project, described in [Anderson et al. \(2008\)](#); we have previously used this software in the search for counterparts to *Chandra* sources in NGC 6397. The reductions were done using an updated version of this software known as KS2. Since our best coverage was in $H\alpha$, we did the first several iterations of star finding on those images. In order to capture very faint stars on both the main sequence and the white dwarf sequence, we followed this with an iteration of star finding using the R_{625} exposures alone and then a final iteration using the B_{435} and R_{625} exposures combined. A total of

68,439 stars were detected in a mosaic that covers the half-mass radius ($115''$) and somewhat beyond, reaching to $150''$ in the corners.

KS2 uses multiple methods for measuring magnitudes. For stars that are well exposed in individual images, we adopted KS2 photometry derived from fitting the PSF to stars in the individual images and averaging the results using sigma clipping to remove outlying values due to cosmic rays, defective pixels, etc. For faint stars, we adopted the KS2 photometry derived from a simultaneous fit of the PSF to all exposures (see [Anderson et al. 2008](#) for details). In the B_{435} and R_{625} bands, photometry was performed separately for the short and long frames.

Photometric calibration to the VEGAMAG system was performed by doing aperture photometry on moderately bright, isolated stars within a $0''.1$ radius aperture, finding the aperture correction to an infinite radius aperture from [Sirianni et al. \(2005\)](#), calculating the median offset between the KS2 photometry and the aperture photometry, and applying the

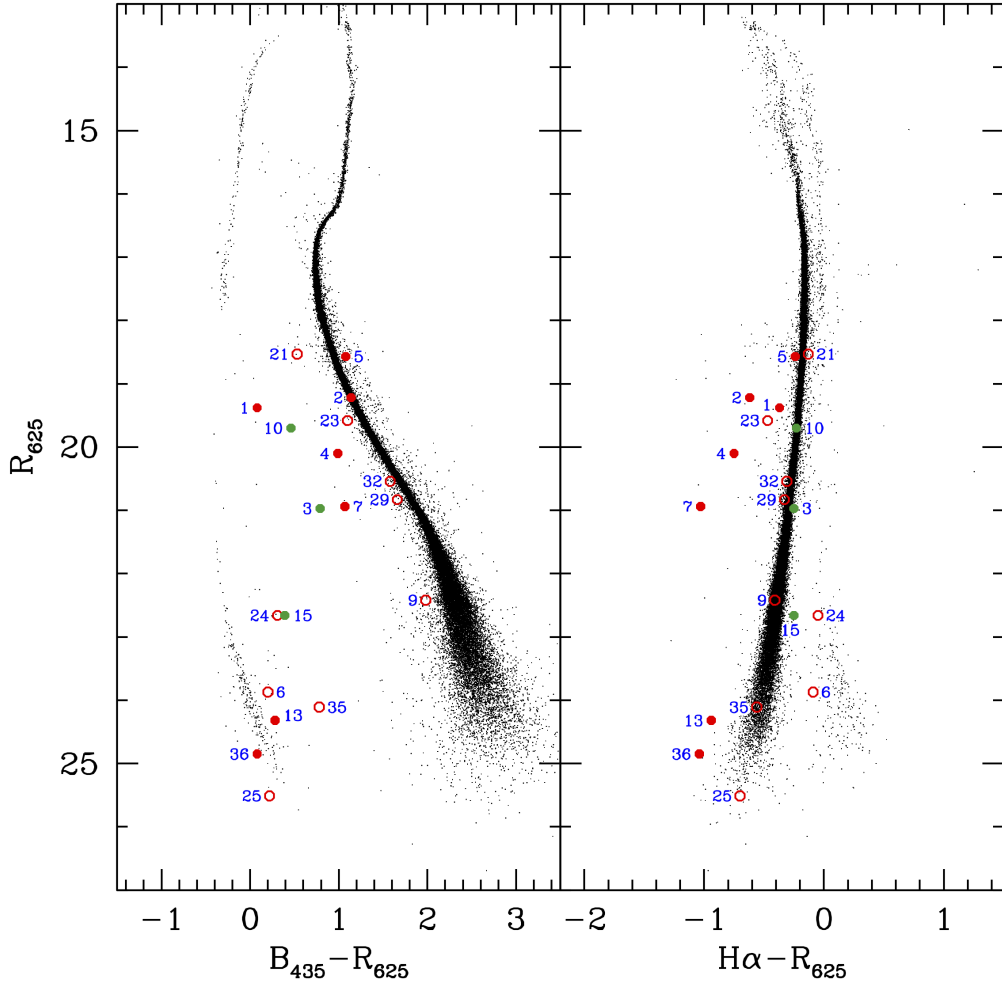


Figure 3. Proper-motion cleaned color-magnitude diagrams for stars within the half-mass radius of NGC 6752 and CV identifications. The candidates have been selected based on their blue color and/or $H\alpha$ excess. Open symbols indicate less certain CV identifications, either due to a weak or absent $H\alpha$ excess and/or uncertain photometry. Note that in the right panel, the bright CVs mostly lie to the $H\alpha$ -excess side of the MS, while the faint CVs mostly lie to the $H\alpha$ -excess side of the WD clump, which itself lies to the $H\alpha$ -deficit side of the MS. All candidate counterparts are shown, independent of their proper-motion status. The counterparts to CX3, CX10, and CX15 have proper motions that are consistent with the extragalactic frame. The counterpart to CX29 has a proper motion that is not consistent with either the cluster frame nor the extragalactic frame. Several other counterparts have undetermined proper motions (see Table 1).

calibrations from the *HST* ACS calibration website.² We produced drizzle-combined mosaic images using the STScI PyRaF routine *astrodrizzle* from the *drizzlepac* package. The drizzle-combined images were oversampled by a factor of two, in order to increase the effective resolution. The resulting supersampled mosaics have an approximately $12,000 \times 12,000$ format and cover an approximately circular field of diameter $5'$ with a pixel scale of $0''.025$. Figures 1 and 2 show the drizzle-combined mosaic of 24 $H\alpha$ frames, together with error circles for the 39 *Chandra* sources within the half-mass radius.

Color-magnitude diagrams (CMDs) were constructed using the R_{625} magnitudes, and the $B_{435} - R_{625}$ and $H\alpha - R_{625}$ color indices. For faint stars ($R_{625} > 21$), we used the photometry derived from simultaneous fits to all of the long exposures. For intermediate-brightness stars ($18 < R_{625} < 21$), we used photometry derived from measurements in individual long exposures. For brighter stars ($R_{625} < 18$), most of which are saturated in the long exposures, we used photometry derived from individual short exposures. The very brightest stars ($R_{625} \lesssim 14.2$) are saturated even in short exposures, and are thus less well measured.

Figures 3 and 4 show the resulting CMDs, where proper-motion cleaning has been applied to filter out field stars (see §3.2). Without proper-motion cleaning, the ($B_{435} - R_{625}$,

² <http://www.stsci.edu/hst/acs/analysis/zeropoints>

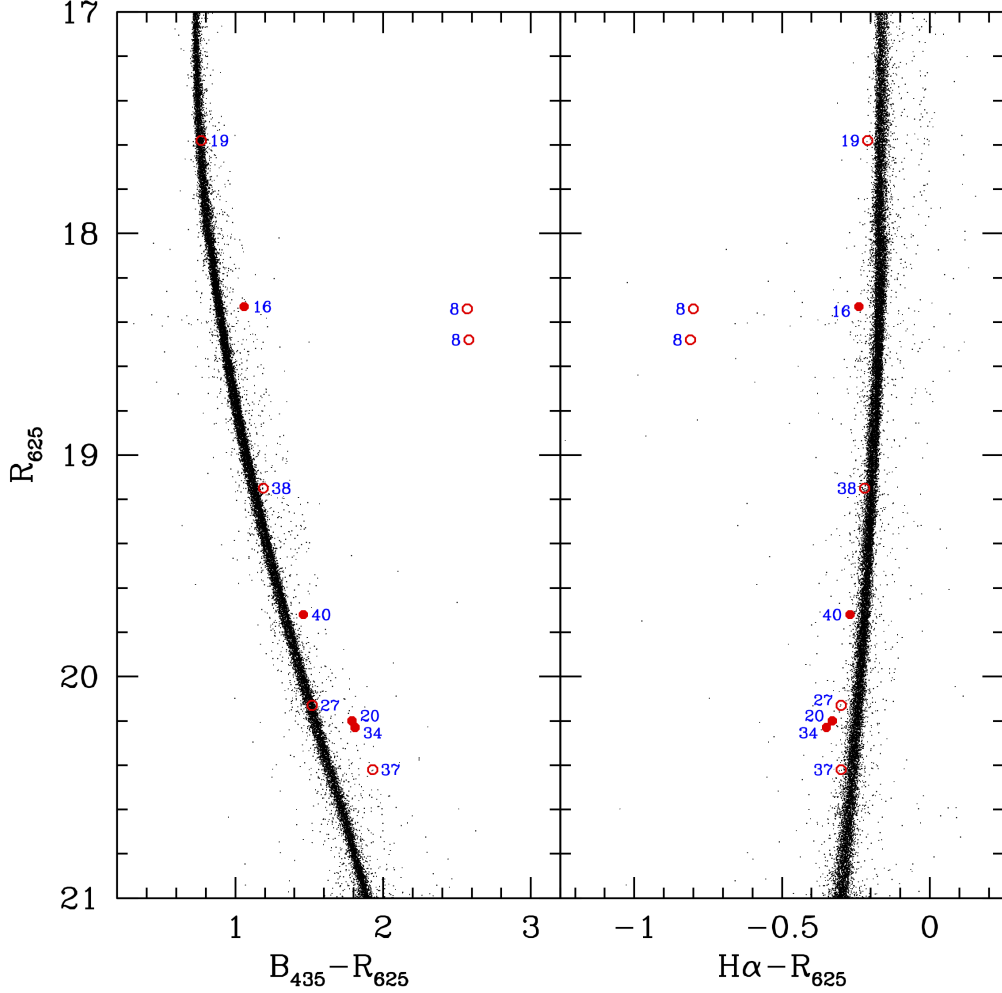


Figure 4. Proper-motion cleaned color-magnitude diagrams for stars within the half-mass radius of NGC 6752 and AB identifications. The candidates have been selected based on their red color and generally small $H\alpha$ excess. All candidate counterparts are shown, independent of their proper motion status. The two counterparts to CX8 have an apparent proper motion that is inconsistent with the cluster mean.

R_{625}) CMD reaches deepest for the bluest stars, since the faintest red main-sequence (MS) stars are below the detection limit in B_{435} . The upper part of the white dwarf (WD) cooling sequence is clearly detected in the $(B_{435} - R_{625}, R_{625})$ CMD, extending to nearly 10 mag below the MSTO in R_{625} . There is also a suggestion of a second WD sequence above the primary carbon-oxygen-core WD sequence, which Hernandez et al. (2013) interpreted as a helium-core WD sequence.

3.2. Astrometry

The drizzle-combined *HST* ACS/WFC mosaic for each filter was rectified to the ICRS using approximately 600 astrometric standards from the USNO UCAC3 catalog. The RMS residual of the plate solution was $0''.09$ in each coordinate. We determined a boresight correction for the *Chandra* source coordinates from Forestell et al. (2014) by computing

the mean offsets between the *HST* and *Chandra* coordinates for three of the brightest CVs from Pooley et al. (2002), viz. sources CX2, CX3, and CX4. The total shift in the coordinates between the *Chandra* and *HST* systems was approximately $0''.1$.

We searched for optical counterparts to the *Chandra* sources by overlaying the *Chandra* error circles on the drizzle-combined *HST* image mosaics, with the boresight correction applied to the *Chandra* source positions from Forestell et al. (2014). Since the uncertainty in the optical positions ($\lesssim 0''.1$) was small compared with the uncertainty in the X-ray positions ($\lesssim 0''.3$), we neglected the contribution of the former to the total positional uncertainty.

In order to test candidate counterparts for cluster membership, we computed proper motion components for all of the objects in the region covered by the image mosaic. The present dataset was used for the reference epoch. We used

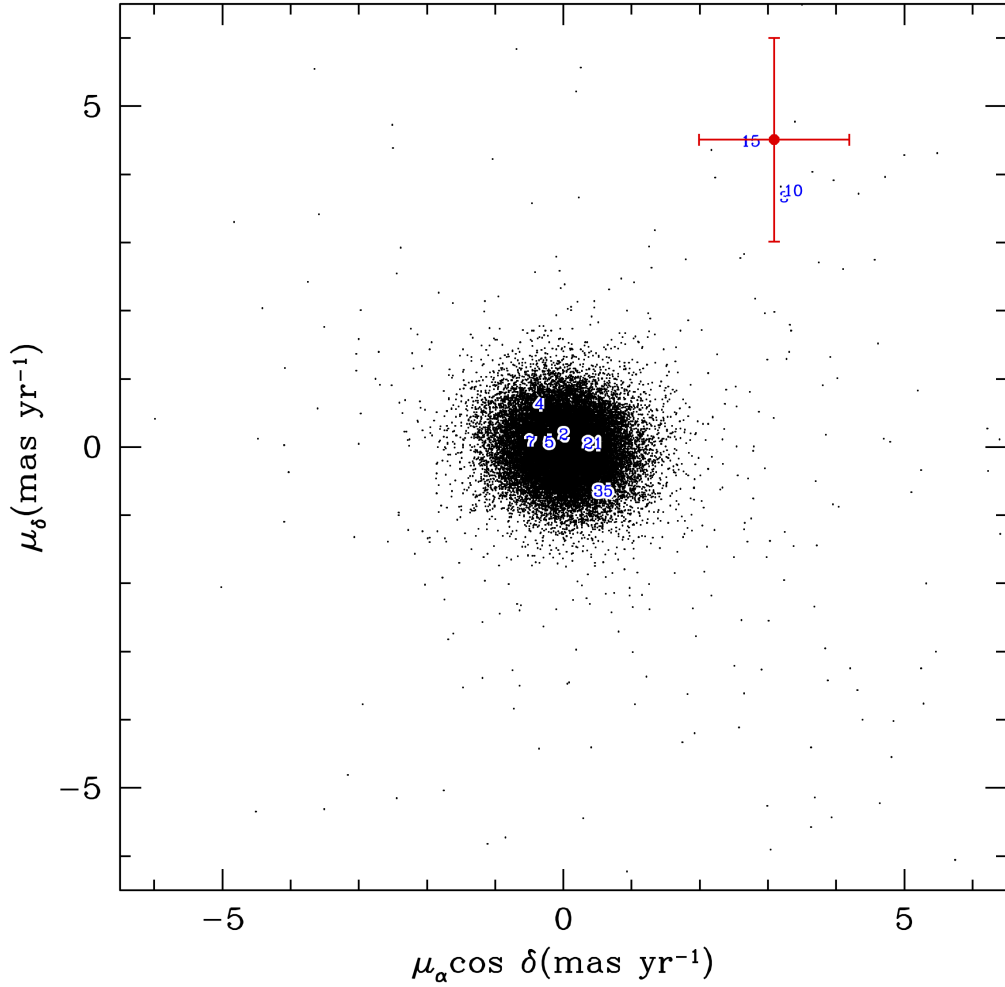


Figure 5. Proper-motion component distribution for stars in the magnitude range $18 \leq R_{625} < 23$. The zero-point corresponds to the systemic cluster motion. The red point and error bars indicate the mean and standard error of the mean of the measured proper motions of eight elliptical galaxies, six of which are in the mosaic field and two of which are in a separate outer field of NGC 6752. The nine objects indicated by blue numbers are initially selected CV candidate counterparts that fall in this magnitude range. The CX2, CX4, CX5, CX7, CX21, and CX35 counterparts are clearly consistent with cluster membership, while the CX3, CX10, and CX15 counterparts have a discordant proper motion that is consistent with the mean galaxy proper motion. We thus interpret these sources as being likely AGNs, as discussed in the text. The CX29 counterpart (not shown) also has a discordant proper motion; however this may well be compromised by the presence of a much brighter neighbor (see Fig. 7).

the GO-10775 (PI: Sarajedini) dataset for the second epoch. It was obtained with the ACS/WFC in 2006 May and covers very nearly all of the half-mass radius region. With a mean epoch for our dataset of 2011 Aug, the two epochs provide a 5.3-year time baseline for proper motion determinations.

The distribution of proper motion components depends on the magnitudes of the stars for which the proper motions are measured, since measurement uncertainties become dominant for the fainter stars. Thus, we compute the amplitude of the proper motion for each of the candidate counterparts and compare it to the RMS proper motion amplitude for stars of similar magnitude. We judge membership to be unlikely for stars with proper motion amplitudes that

exceed the RMS amplitude by more than a factor of three. Figure 5 shows the proper motion component distribution for stars in the wide magnitude range $18 \leq R_{625} < 23$, with the nine initially selected CV candidates in this range with measured proper motions indicated. Six of the candidates have proper-motion amplitudes that are clearly consistent with membership, while three—the counterparts to CX3, CX10, and CX15—are clearly discordant. It is striking that these three objects have nearly the same proper motion, suggesting that they might, in fact, be background active galactic nuclei (AGNs).

To investigate this possibility, we determined the absolute proper motion of NGC 6752 by locating a sample of galaxies

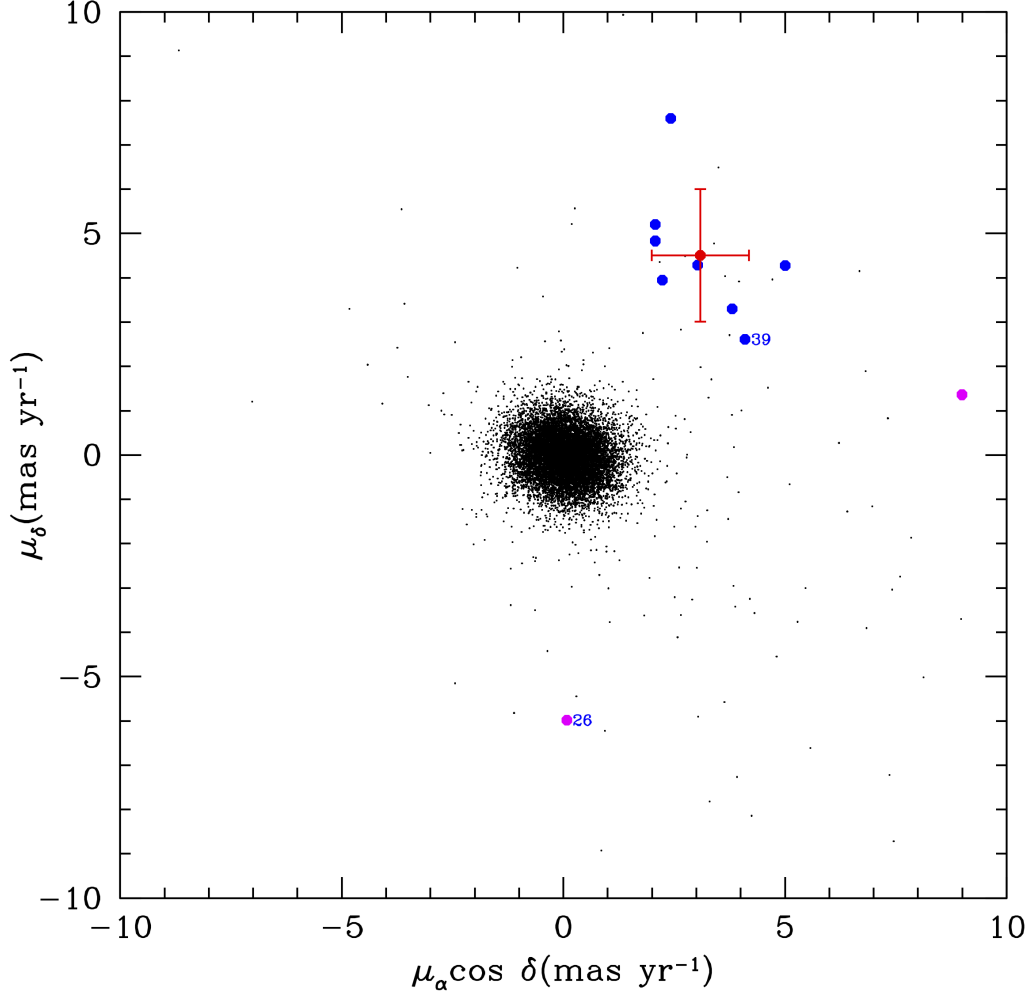


Figure 6. Proper-motion component distribution for stars in the magnitude range $21 \leq R_{625} < 23$ with the proper motions of 10 galaxies overplotted as blue and magenta dots. The zero-point corresponds to the systemic cluster motion. The red point and error bars indicate the mean and standard error of the mean of the eight brightest galaxies (blue dots), six of which are in the mosaic field and two of which are in a separate outer field of NGC 6752. The two faintest galaxies (magenta dots) have discordant proper motions relative to the clump defined by the eight brightest galaxies and thus were not included in the average. The two numbered dots are the candidate counterparts to sources CX26 and CX39 (see Fig. 7).

in our image mosaic and also in an outer field that was imaged by the ACS/WFC in 2004 and 2012. We used the SExtractor software (Bertin & Arnouts 1996) to detect objects in both fields and filtered the list of detected objects on a combination of “stellarity” index, ellipticity, PSF FWHM, and the difference between the maximum surface brightness and the Kron magnitude³ to generate a list of candidate galaxies. This list includes both galaxies and bright-star PSF artifacts. In order to filter out the later, we visually inspected each of the several hundred galaxy candidates and selected the obvious galaxies. This resulted in a list of 10 galaxies with mea-

sured proper motions, eight in the central region and two in the outer region. The result of this analysis is shown in Figure 6, where the galaxy proper motions are overplotted on the distribution of proper motions for all objects in the magnitude range $21 \leq R_{625} \leq 23$. With the exception of two outliers, the galaxies fall in a compact clump, which defines the absolute proper-motion zero-point. The two outliers are, in fact, the faintest two galaxies in the sample and thus likely have the least reliably determined proper motions. The mean galaxy proper motion is plotted in both Figs. 5 and 6. It is clear from these figures that the proper motions of the proposed counterparts to CX3, CX10, and CX15 agree with the galaxy mean. Given this agreement in proper motion, it appears highly likely that CX3, CX10, and CX15 are actually background active galactic nuclei (AGNs) rather than CVs in

³ This difference measures the central concentration of the object image and provides another means of star/galaxy discrimination (Annunziatella et al. 2013).

the cluster. Further evidence for this interpretation is given in §4.2.

4. RESULTS

4.1. Chandra Source Identification

We used the optical CMDs to detect likely *Chandra* source counterparts and investigate their properties. For each of the 39 *Chandra* sources within the half-mass radius, we checked the CMD locations of all objects that fell within a distance

of the maximum of 2.5 times the error circle radius and $0''.3$. The rationale for choosing this search region size is that the formal p_{detect} error circle radii are quite small for the brightest sources ($\sim 0''.02$) and in some of these cases potential candidates were located near, but not within, the actual error circle. We note that [Hong et al. \(2005\)](#) have observed that wavelet detection algorithms systematically underestimate positional uncertainty. Their prescription for determining 95% positional uncertainty produces an asymptotic lower-limiting value of about $0''.3$ for an on-axis source.

Table 1. Optical Counterpart Summary

Source ^a	RA, Dec (J2000) ^b	r_{err} ($''$) ^c	r ($''$) ^d	N_{detect} ^e	Offset ^f	Type ^g	PM ^h	R_{625}	B_{435}	H α	Notes
CX1	19:10:51.138 – 59:59:11.92	0.01	0.17	2	1.8	CV	...	19.38	19.46	19.01	
CX2	19:10:56.005 – 59:59:37.33	0.02	0.73	1	1.0	CV	c	19.22	20.36	18.60	
CX3	19:10:40.375 – 59:58:41.47	0.02	1.52	1	1.3	AGN	f	20.97	21.76	20.72	
CX4	19:10:51.586 – 59:59:01.73	0.02	0.08	2	0.8	CV	c	20.10	21.09	19.35	
CX5	19:10:51.414 – 59:59:05.18	0.02	0.09	1	1.6	CV?	c	18.57	19.65	18.33	
CX6	19:10:51.505 – 59:59:27.10	0.03	0.38	1	0.8	CV?	...	23.87	24.07	23.78	very blue, small H α excess
CX7	19:10:51.511 – 59:58:56.85	0.02	0.15	2	1.9	CV	c	20.94	22.01	19.91	
CX8	19:11:02.969 – 59:59:41.92	0.05	1.49	3	5.3	AB?	...	18.34	20.91	17.54	two red, H α -excess objects
CX8				3 ⁱ	6.4	AB?	...	18.48	21.06	17.67	
CX9	19:10:51.766 – 59:58:59.25	0.04	0.10	2	3.0	CV?	...	22.42	24.40	22.01	somewhat blue, H α excess in color-color diagram
CX10	19:10:54.754 – 59:59:13.86	0.06	0.37	1	1.2	AGN	f	19.70	20.16	19.47	
CX11	19:10:52.408 – 59:59:05.64	0.08	0.04	2	counterpart suggested by Pooley et al. (2002) is not detected; only MS stars present in search area; MSP D
CX13	19:10:40.610 – 60:00:05.91	0.14	1.76	1	1.0	CV	c	24.32	24.60	23.38	
CX14	19:10:52.063 – 59:59:09.09	0.08	0.08	2	only MS stars present in search area
CX15	19:10:55.847 – 59:57:45.78	0.08	1.39	1	1.0	AGN	f	22.66	23.05	22.41	
CX16	19:10:42.531 – 59:58:43.03	0.13	1.25	1	1.1	AB	c	18.33	19.39	18.09	
CX17	19:11:05.258 – 59:59:04.42	0.16	1.65	1	...	GLX	asymmetric, extended object; photometry not possible
CX18	19:10:52.056 – 59:59:03.71	0.14	0.02	2	only MS stars present in search area
CX19	19:10:55.600 – 59:59:17.33	0.16	0.49	3	1.8	AB?	c	17.58	18.35	17.37	normal $B_{435} - R_{625}$, small H α excess
CX20	19:10:52.848 – 59:59:02.54	0.10	0.10	1	2.7	AB	c	20.20	21.99	19.87	
CX21	19:10:49.516 – 59:59:43.16	0.11	0.72	2	0.7	CV?	c	18.53	19.06	18.40	blue, small H α excess in color-color diagram
CX22	19:11:02.950 – 59:57:58.91	0.13	1.74	0	empty search region
CX23	19:10:52.546 – 59:59:04.38	0.11	0.06	4	0.4	CV?	c	19.58	20.68	19.11	uncertain photometry
CX24	19:10:52.670 – 59:59:03.21	0.12	0.07	4 ⁱ	3.4	CV?	...	22.66	22.97	22.61	weakly detected in R_{625} and H α
CX25	19:10:51.957 – 59:58:40.55	0.13	0.40	5 ⁱ	3.9	CV?	...	25.51	25.73	24.81	weakly detected in R_{625} and H α
CX26	19:10:39.162 – 59:59:45.15	0.23	1.75	2	1.9	GLX	f	23.00	25.16	22.55	extended elliptical image
CX27	19:10:52.059 – 59:59:00.84	0.12	0.06	1 ⁱ	3.7	AB?	c	20.13	21.65	19.83	normal $B_{435} - R_{625}$, small H α excess; MSP B
CX28	19:10:42.509 – 59:59:44.46	0.22	1.37	0	empty search region

Table 1 continued

Table 1 (continued)

Source ^a	RA, Dec (J2000) ^b	r_{err} (") ^c	r (") ^d	N_{detect} ^e	Offset ^f	Type ^g	PM ^h	R_{625}	B_{435}	H α	Notes
CX29	19:10:52.293 – 59:59:01.79	0.16	0.05	4	0.4	CV?	f	20.83	22.49	20.50	slightly blue, small H α excess
CX30	19:10:40.678 – 59:58:39.61	0.19	1.49	0	faint object in wings of much brighter star; not detected by KS2
CX31	19:10:50.514 – 59:57:37.11	0.17	1.47	1	only red giant present in search area
CX32	19:10:54.137 – 59:59:11.04	0.17	0.28	1	1.7	CV?	...	20.54	22.12	20.23	slightly blue, slight H α excess
CX33	19:11:03.287 – 59:58:01.31	0.19	1.75	0	empty search region
CX34	19:10:45.694 – 59:58:20.09	0.20	1.09	1	1.6	AB	c	20.23	22.04	19.88	
CX35	19:10:52.165 – 59:59:16.73	0.19	0.20	2	0.4	CV?	...	24.11	24.89	23.35	uncertain photometry
CX36	19:10:49.585 – 59:58:26.41	0.20	0.71	1	2.2	CV	...	24.85	24.93	23.81	
CX37	19:10:50.509 – 59:59:08.77	0.21	0.21	4	1.1	AB?	c	20.42	22.35	20.12	somewhat red, no H α excess in color-color diagram
CX38	19:11:02.151 – 59:58:11.81	0.24	1.53	1	1.4	AB?	c	19.15	20.34	18.93	slightly red, slight H α excess
CX39	19:10:46.352 – 59:57:49.92	0.22	1.44	1	1.8	GLX	f	22.26	24.86	21.89	extended elliptical image
CX40	19:10:50.357 – 59:59:13.89	0.27	0.27	7	2.2	AB	c	19.72	21.18	19.45	

^a From [Forestell et al. \(2014\)](#).

^b *Chandra* source positions from [Forestell et al. \(2014\)](#) have been boresight-corrected to align with the drizzled image coordinate system, which is tied to the ICRS.

^c Wavdetect error circle radius in arcsec. The search area radius is $\max(2.5 r_{\text{err}}, 0.3'')$.

^d Projected distance from cluster center in arcmin.

^e Number of objects detected within $\max(2.5 r_{\text{err}}, 0.3'')$.

^f Offset of counterpart from X-ray position in units of r_{err} .

^g CV = cataclysmic variable; CV? = less certain CV identification for reason noted in table; AB = active binary candidate; AB? = less certain AB identification for reason noted in table; GLX = galaxy; AGN = active galactic nucleus.

^h Proper-motion membership: c = consistent with cluster; f = consistent with field; ... = no proper-motion measurement.

ⁱ Preferred counterpart lies somewhat outside of formal search region.

Objects that fell on the main sequence, subgiant branch, or giant branch were considered to be unlikely counterparts, given the relatively low X-ray to optical flux ratio, f_X/f_{opt} , of such stars, in contrast to the ranges for chromospherically active binaries and cataclysmic variables. Table 1 summarizes the result of this counterpart search. Figure 7 shows finding charts for identifications that have changed or are new since the previous studies by [Pooley et al. \(2002\)](#) and [Thomson et al. \(2012\)](#).

4.2. Source Types

Based on the location of the proposed counterparts in the CMDs, we primarily assigned types of candidate cataclysmic variable (CV) and candidate chromospherically active binary (AB). Candidate CVs were generally identified by being significantly to the blue of the MS and/or having large H α excesses (either relative to the MS or to the WD sequence). ABs were defined as lying within ~ 0.75 mag above the MS (and thus within ~ 0.2 mag to the red of the MS) and having small H α excesses ($\lesssim 0.1$ mag), based on our previous analysis of ABs in NGC 6397 ([Cohn et al. 2010](#)).

Although our proposed counterpart to CX5 lies slightly to the red side of the MS, its high $L_X = 1.1 \times 10^{32}$ erg s $^{-1}$ and

moderately high $f_X/f_{\text{opt}} = 1.4$ tend to support its identification as a CV. One possibility is that the object detected at the position of CX5 is a MS star that is covering up the much fainter true counterpart. However, examination of the stellar image does not indicate any obvious asymmetry. Given the weak H α excess of CX5, we include it among the less certain CV identifications.

In cases where only MS stars were present in the search region (viz. CX11, CX14, CX18, and CX35) and in one case where a red giant was present in the search area (CX31), we noted this in Table 1 and did not assign a counterpart. We note that an AB with a low mass ratio and weak lines could look like a MS star in both CMDs. In some of these cases, it may be that a bright star near the *Chandra* source location is covering up a much fainter star.

Three objects, viz. sources CX17, CX26, and CX39, were classified as background galaxies, based on the extended appearance of their images. The R_{625} -band images of the source CX26 and CX39 counterparts resemble elliptical galaxies in appearance, with a smooth elongation. The image of the source CX17 counterpart has a more complex structure, possibly suggestive of interacting galaxies. The two

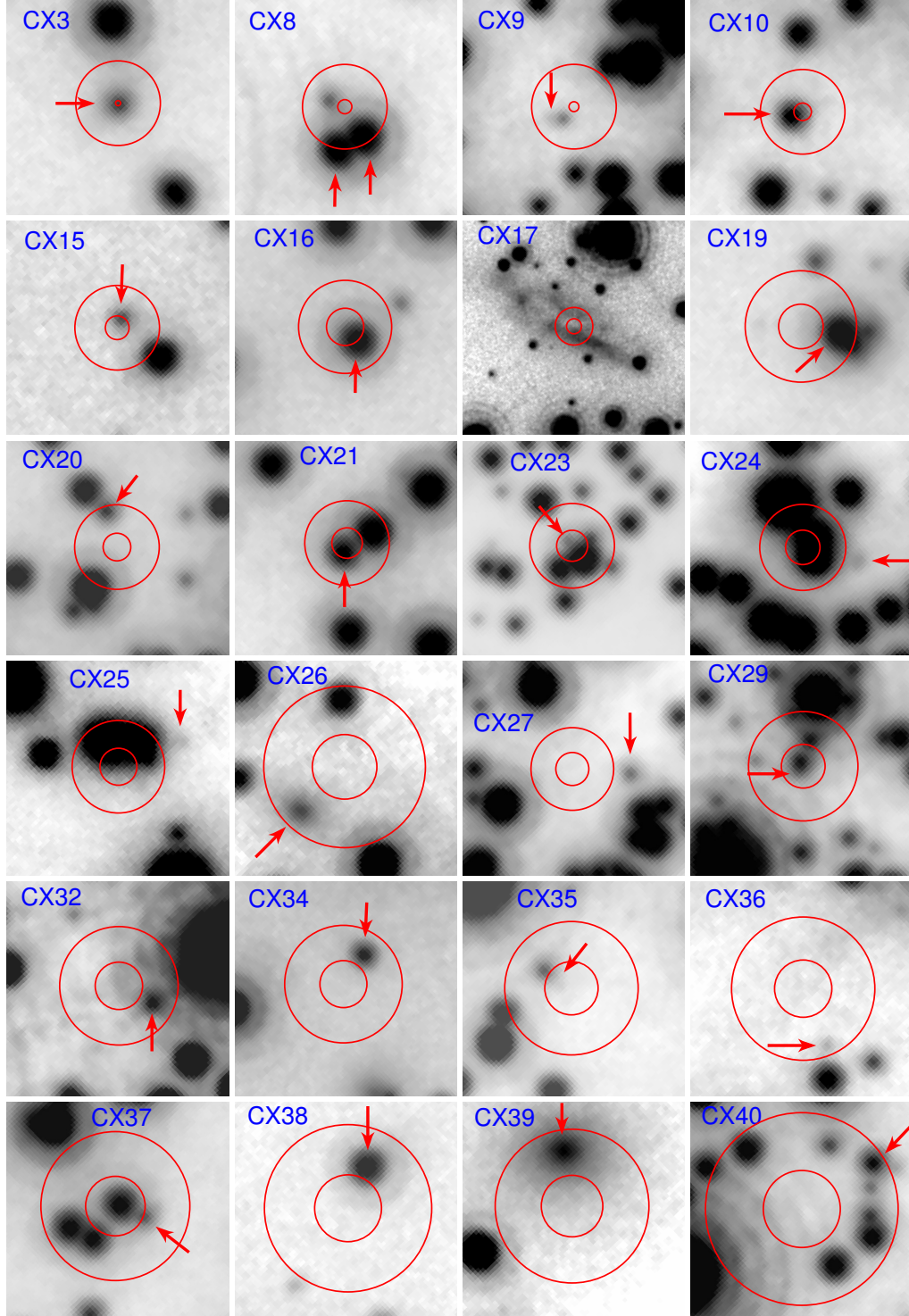


Figure 7. Finding charts for revised and new source identifications. All charts are for the $H\alpha$ band, with the exception of those for sources CX24 and CX25, which are for the B_{435} band, in which the counterpart was more strongly detected. North is up and east is to the left. With the exception of the chart for CX17, the regions shown are $1''.5 \times 1''.5$. For CX17, the region is $4''.5 \times 4''.5$. The inner circles represent the formal error circle and the outer circles represent the search regions, which have a radius of the maximum of $2.5 r_{\text{err}}$ and $0''.3$. The arrows point to the candidate counterparts. As discussed in §§3.2 and 4.2, the counterparts to CX3, CX10, and CX15, which were previously classified as CVs, now appear to be AGN, based on their proper motions and lack of an $H\alpha$ excess.

apparent elliptical galaxies have moderate X-ray to optical flux ratios of $\sim 0.3 - 1$, consistent with normal galaxies (see §4.5). It was not possible to perform PSF-fitting photometry on the source CX17 counterpart, given its rather amorphous structure, without a central nucleus, and thus we did not compute an X-ray to optical flux ratio for it. As noted by Pooley et al. (2002), this source coincides with a radio source, which further supports its identification as a galaxy.

Three objects that have been previously classified as CVs, viz. sources CX3, CX10, and CX15, were ultimately classified as background AGNs, based on their proper motions, which are discordant from the cluster distribution but in agreement with the galaxy mean (which included the proper motion of the counterpart to CX39).⁴ The deep imaging in this study indicates that these three source counterparts are pointlike, without any hint of extension. This is consistent with an AGN interpretation. As can be seen in Fig. 10, these three sources have moderate to high X-ray to optical flux ratios of $\sim 0.3 - 20$, consistent with AGNs. Examination of the $(H\alpha - R_{625}, R_{625})$ CMD indicates that the counterparts to these three sources do not show an $H\alpha - R_{625}$ excess although all three counterparts are blue in the $(B_{435} - R_{625}, R_{625})$ CMD. This is further evidence for the AGN interpretation, as AGN would not be expected to show a zero-redshift $H\alpha$ excess.

Figure 3 shows the location of the likely or less certain CV candidates in the CMDs. As we noted in Cohn et al. (2010) for the CV population in NGC 6397, there is a brighter group of CV candidates that generally lie blueward of the main sequence in $B_{435} - R_{625}$ and generally show $H\alpha$ excesses, and a fainter group of CV candidates that are distributed around the WD cooling sequence in the $(B_{435} - R_{625}, R_{625})$ CMD and generally show $H\alpha$ excesses relative to the WD sequence. All but two of the 11 brightest CV candidates lie 0.1 – 1.3 mag to the blue of the MS in the $(B_{435} - R_{625}, R_{625})$ CMD; the candidate counterpart to source CX2 lies on the MS and the counterpart to CX5 lies slightly to the red of the MS. As we noted in Cohn et al. (2010), the optical emission of the bright CV systems appears to be dominated by the secondary in the R_{625} band, with a larger contribution from the disk in the B_{435} band. The fairly high R_{625} -band fluxes indicate that the secondaries are relatively massive, $\sim 0.5 - 0.7 M_{\odot}$. Five of the nine brightest CV candidates, viz. sources CX1, CX2, CX4, CX7, and CX23, show $H\alpha$ excesses of 0.2 – 0.8 mag relative to the MS. Of the remaining four bright CV candidates, sources CX5, CX29, and CX32 show a small $H\alpha$ excess, and source CX21 is slightly to the $H\alpha$ deficit side of the MS. Though CX21 does not show a

$H\alpha$ excess, its proper motion verifies that it is a cluster member, and therefore cannot be an AGN. Further investigation of the $H\alpha$ -status of the proposed CV counterparts using the color-color diagram is described below.

About 1.5 mag below the faintest of the bright CV candidates are two possible transitional objects, the counterparts to sources CX9 and CX24. The candidate counterpart to CX9 has a small $B_{435} - R_{625}$ excess and lies on the MS in the $(H\alpha - R_{625}, R_{625})$ CMD. The candidate counterpart to CX24 lies near the WD regions in both the $(B_{435} - R_{625}, R_{625})$ and $(H\alpha - R_{625}, R_{625})$ CMDs.

About 1.5 mag below the proposed CX9 and CX24 counterparts lie five faint CV candidates. These fall on or near the WD sequence in the $(B_{435} - R_{625}, R_{625})$ CMD. Four of the five, viz. the counterparts to sources CX13, CX25, CX35, and CX36, show $H\alpha$ excesses relative to the normal WD sequence in the $(H\alpha - R_{625}, R_{625})$ CMD. The fourth faint CV candidate, source CX6, is found among the main distribution of white dwarfs in its $H\alpha - R_{625}$ color index. As we noted in Cohn et al. (2010), the optical fluxes for the faint CV candidates in NGC 6397 are dominated by the contribution of the WD. The $H\alpha$ excess that four of the five faint CV candidates show relative to the WD distribution suggests that the faint CVs have a strong $H\alpha$ -emission core (due to an accretion disk) within the broad absorption lines of the WD continuum.

The five faint CV candidates in NGC 6752 are clustered near $R_{625} \sim 24.5$, which corresponds to $M_R \sim 11.4$, which is similar to the magnitude of the clump of faint CVs observed in NGC 6397. As we noted, this characteristic magnitude is also similar to that of the sharp peak in the field CV distribution observed in the Sloan Digital Sky Survey by Gänsicke et al. (2009). The peak in the field distribution occurs near the CV period minimum ($P \approx 80 - 86$ min). Thus, it appears likely that the faint CVs that we are observing in NGC 6752 also correspond to the period-minimum population. We can also compare the X-ray luminosity to detailed simulations of CV evolution in globular clusters. We use the simulations of Ivanova et al. (2006), which predict the optical and X-ray flux of CVs in globular clusters throughout their evolution. In the range $M_V = 11 - 12$, we find that 80% of their simulated CVs are predicted to have periods below the period gap, but not yet increasing in period, with small numbers of CVs above the period gap, “period-bouncers” with degenerate hydrogen-rich companions, and AM CVn stars. The predicted L_X range for these populations is $L_X(0.5 - 8 \text{ keV}) = 5 \times 10^{29} - 3 \times 10^{31} \text{ erg s}^{-1}$, and the median L_X is $\sim 4 \times 10^{30} \text{ erg s}^{-1}$; these well match the L_X range of these five candidate faint CVs, $7 \times 10^{29} - 5 \times 10^{31} \text{ erg s}^{-1}$, and their median of $2 \times 10^{30} \text{ erg s}^{-1}$ (from Forestell et al. 2014).

Further insight into the $H\alpha$ -status of the CV candidates NGC 6752 is provided by the color-color diagram, Fig. 8.

⁴ The counterpart to CX26 has a discordant proper motion from the eight galaxies used to calculate the galaxy mean. We attribute this to a poorly determined proper motion for this object.

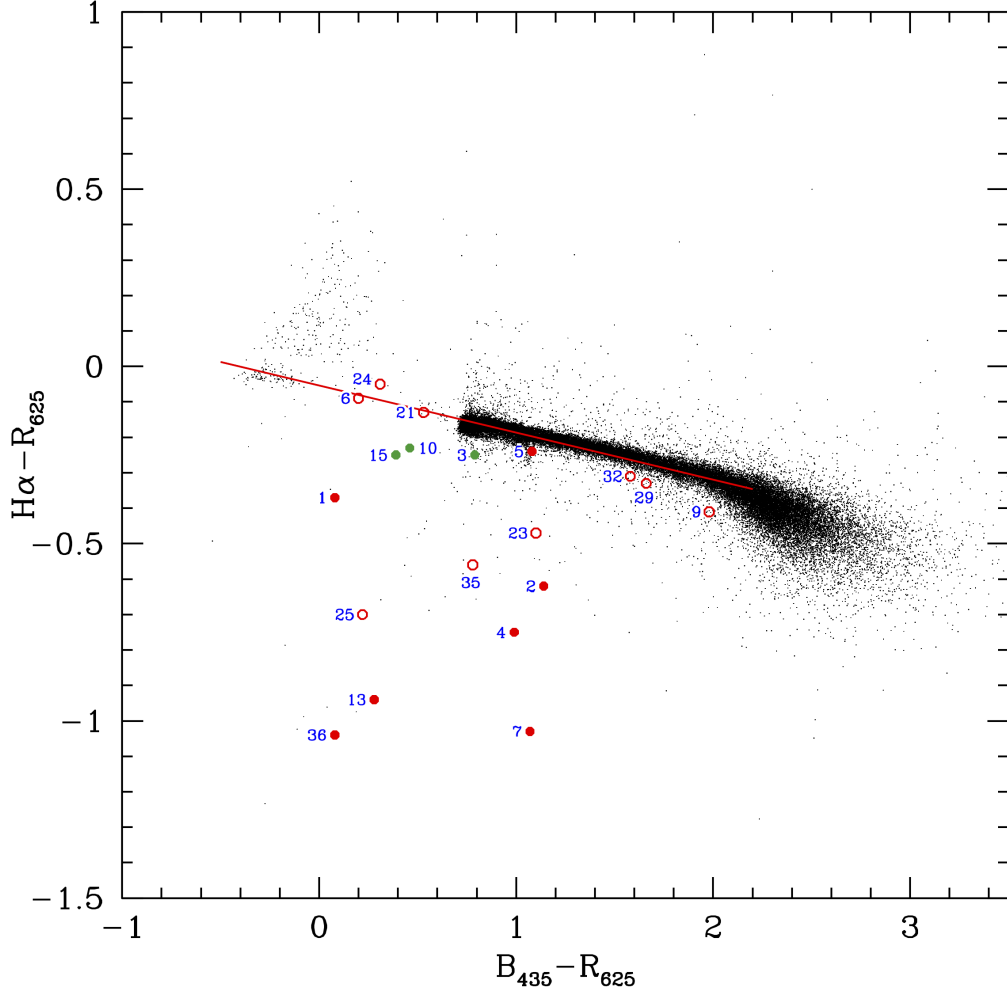


Figure 8. Proper-motion cleaned color-color diagram for stars within the half-mass radius of NGC 6752 and CV identifications. The candidates are the same as in Fig. 3. Open symbols indicate less certain CV identifications. The red line is a linear regression of $H\alpha - R_{625}$ on $B_{435} - R_{625}$ over the range $-0.5 \leq B_{435} - R_{625} \leq 2.2$. All stars brighter than $R_{625} = 15.5$ have been excluded, since saturation effects set in at the bright end. The blue end of the color-color relation is populated by stars on the extreme blue horizontal branch. Note that all of the candidates except the counterpart to CX24 lie below (i.e. to the $H\alpha$ -excess side of) the color-color relation.

It can be seen that there is a nearly linear relation between the two colors, as indicated by the red line that represents a linear regression of $H\alpha - R_{625}$ on $B_{435} - R_{625}$ over the range $-0.5 \leq B_{435} - R_{625} \leq 2.2$. All of the proposed counterparts, with the exception of those to sources CX6, CX21, and CX24, fall significantly below the relation. Thus, in some cases where the candidate does not lie to the $H\alpha$ -excess side of the MS in the $(H\alpha - R_{625}, R_{625})$ CMD, it still shows a significant $H\alpha$ -excess relative to other objects of its $B_{435} - R_{625}$ color. The proposed counterparts to CX6 and CX21 fall very slightly to the $H\alpha$ -excess side of the color-color relation, while the proposed counterpart to CX24 falls a small distance to the $H\alpha$ -deficit side of the relation, though all three counterparts are consistent with the MS color-color

relation, within the $H\alpha - R_{625}$ scatter at their R_{625} magnitudes (~ 0.1 mag at CX24's $R_{625} = 22.66$).

We can think of several scenarios to explain these systems without clear $H\alpha$ excesses or deficits. There might be only small $H\alpha$ emission, which is not strong enough to dominate over the $H\alpha$ absorption. For example, CX21 might be interpreted as a bright, nova-like CV, with an accretion flow that is mostly optically thick, leading to weak $H\alpha$ emission. Perhaps there is no accretion disk, which would suggest a radio millisecond pulsar nature. CX24 indeed has a small X-ray luminosity and soft X-ray color, consistent with the X-rays from most radio millisecond pulsars (e.g. [Bogdanov et al. 2011](#)). However, CX6 is brighter and has a harder X-ray spectrum. This is consistent with radio millisecond pulsars showing strong shocks, the redbacks and black widows (e.g.

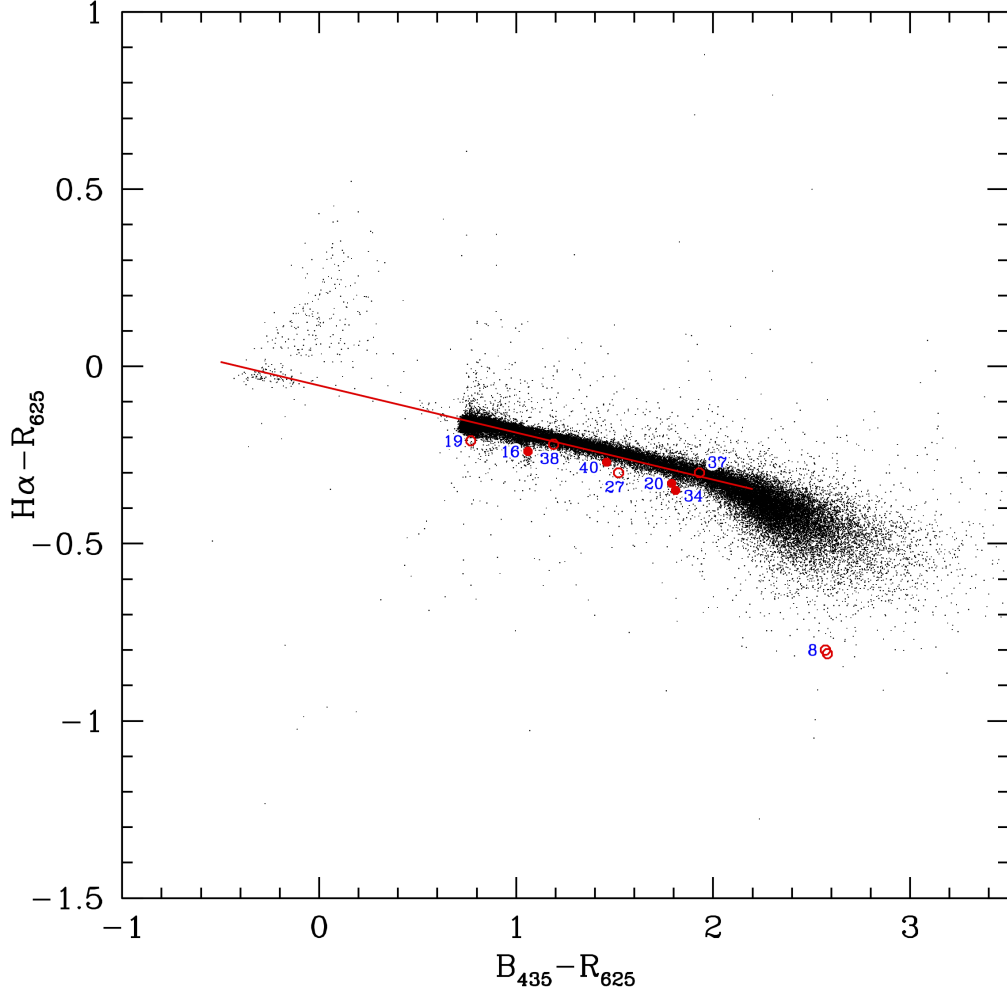


Figure 9. Proper-motion cleaned color-color diagram for stars within the half-mass radius of NGC 6752 and AB identifications. The candidates are the same as in Fig. 4. Note that all of the candidates except the counterpart to CX37 lie below (i.e. to the $H\alpha$ -excess side of) the color-color relation.

Gentile et al. 2014; Bogdanov et al. 2010), but the optical data show a He WD companion, apparently ruling out a millisecond pulsar nature for CX6. CX21’s optical counterpart, however, is consistent with a redback millisecond pulsar, as is its low X-ray luminosity and moderately soft hardness. Finally, any or all of these three objects could be AM CVn stars, where a He WD (that has lost its outer H layer) donates mass to (typically) a CO WD. In such a system, optical flux could come from the accreting WD and/or the accretion disk, neither of which would show hydrogen lines in emission or absorption. Such systems have been predicted to be present in globular clusters (e.g. by Ivanova et al. 2006) and evidence for the detection of an AM CVn binary in NGC 1851 has been presented by Zurek et al. (2016).

Figure 4 shows the location of the objects identified as AB stars in the CMDs. As in NGC 6397, these objects sometimes lie close to the edge of the MS in either the right or left panel, but deviate from the MS by a larger amount in the

other panel. Of the nine AB counterparts listed in Table 1, eight are newly identified in our study. This increase in the detection rate appears to result both from the deeper *Chandra* imaging dataset that we used, compared with that of Pooley et al. (2002), and the increased photometric precision possible with the ACS/WFC vs. the WFPC2, which allows us to identify objects that deviate by small amounts from the MS. As seen in NGC 6397 and 47 Tuc, the ABs are likely to be a mixture of BY Draconis stars, W Ursa Majoris stars, and other contact binaries (see Albrow et al. 2001; Taylor et al. 2001; Cohn et al. 2010).

Figure 9 shows the location of the objects identified as AB stars in the color-color diagram. As can be seen in the figure, all of the AB candidates except for the counterpart to CX37 fall below the line that represents the linear regression to the color-color relation. As in NGC 6397, the $H\alpha$ excesses of the AB candidates are typically much smaller than those of the CV candidates. This is consistent with the findings of Kafka

& Honeycutt (2006) and Beccari et al. (2014) that chromospherically active binaries do not show $H\alpha$ equivalent widths in excess of about 10 \AA . An apparent exception is the object pair that is the proposed counterpart to CX8, which falls well below the linear regression, as discussed and explained below.

The faintest ABs that are detected in the X-ray in NGC 6752 have $R_{625} \approx 20.5$, corresponding to $M_R \approx 7.4$. At this magnitude, we reach the X-ray detection limit of $L_X \approx 5 \times 10^{29} \text{ erg s}^{-1}$. In contrast, the AB sequence that we detected in NGC 6397 reaches a deeper limit of $M_R \approx 9.7$, owing to the deeper X-ray detection limit of $L_X \approx 9 \times 10^{28} \text{ erg s}^{-1}$. Given deeper X-ray imaging, it should be possible to trace the AB sequence farther down the MS of NGC 6752. New, deeper *Chandra* observations are now scheduled for 2017.

Our proposed counterpart to source CX8 stands out for its very red color and large apparent $H\alpha$ excess. There are actually two photometrically similar stars located $0''.2$ apart, within about $0''.3$ of the X-ray source position (see Fig. 7; the photometry for these stars is plotted in Fig. 4). We found similarly discordant stars in NGC 6397 and interpreted them as likely foreground ABs superposed on the cluster, with distance moduli that put them well above the fiducial sequences in the CMDs (Cohn et al. 2010, see their §4.2 and Fig. 4). The vertical offset for the possible CX8 counterparts, roughly estimated at $3.6 - 4.6$ magnitudes (taking into account the opposite effects of metallicity and reddening on NGC 6752 stars), suggests a distance $5 - 8$ times closer, or $500 - 800 \text{ pc}$. At this distance, the two stars are $100 - 160 \text{ AU}$ in projection from each other, making them likely to be bound, but the separation is much too large to produce chromospheric activity. One possible explanation for the activity is that the two stars are both unresolved binaries. A plausible explanation (which we explore further below) is that the two stars are each an unresolved binary. (We note that explaining the activity as due to youth is rather unlikely, since only a tiny fraction of field M stars are likely to be young enough to have substantial chromospheric activity, while many M stars are likely to reside in tight binaries.)

We note that even without actual $H\alpha$ emission, M star spectra have a peak at the location of the $H\alpha$ line, owing to the presence of TiO bands to either side of this wavelength. We have used the *synphot* utility in IRAF/STSDAS to estimate the apparent $H\alpha - R_{625}$ excess for a normal M5V star as a function of metallicity. We used the Castelli & Kurucz (2004) spectra for metallicity values of -1.5 (appropriate to NGC 6752), 0.0 (solar), and 0.5 (super solar), with $T_{\text{eff}} = 3500 \text{ K}$ and $\log(g) = 5.0$. The predicted values of $H\alpha - R_{625}$ for these three metallicities are -0.41 , -0.58 , and -0.59 , respectively. We note that our proposed counterparts to CX8 have a $H\alpha - R_{625}$ value of -0.80 , suggesting that

there is some actual $H\alpha$ emission, although about 75% of the apparent $H\alpha - R_{625}$ excess can be accounted for as a consequence of the spectral features of a normal mid-M dwarf star that is part of the disk population. We calculated an equivalent width (EW) corresponding to the residual $H\alpha - R_{625}$ excess of -0.2 , following the procedure of Beccari et al. (2014), finding a value of $\text{EW}(H\alpha) = 13 \text{ \AA}$. This is similar to the values they found for early M stars registering an $H\alpha$ excess in 47 Tuc.

While the two stars do not have a formal proper motion determination from KS2, it is clear from direct measurement that they have a similar and quite substantial proper motion, about 27 mas yr^{-1} . For the distance range of $500 - 800 \text{ pc}$ estimated above, this corresponds to a transverse velocity of $64 - 100 \text{ km s}^{-1}$. This is a high velocity range for the thin disk of the Galaxy, but is consistent with the velocity range for the thick disk (Binney & Merrifield 1998, p. 656).

We can gain further information about CX8 from the combined X-ray spectrum and flux. Pooley et al. (2002) noted that it has a very soft spectrum, and suggest a millisecond pulsar nature cannot be excluded. Heinke et al. (2003) suggested that the spectrum showed evidence for an emission line, and that a foreground AB nature was the most likely explanation for this system. We have performed spectral fits to the combined Chandra data, extracted as described in Forestell et al. (2014), grouping by 15 counts/bin. We find that fitting power law or hydrogen neutron star atmospheres (NSATMOS, Heinke et al. 2006) with the cluster N_H provides unacceptably poor fits. Thawing the N_H allows decent fits, though we then find $N_H = 3.3^{+0.8}_{-0.7} \times 10^{21} \text{ cm}^{-2}$ for the NSATMOS fit, which is 10 times higher than the cluster value, which would be difficult to explain for a millisecond pulsar nature. A single MEKAL model (Liedahl et al. 1995) gives an unacceptable fit, but a double MEKAL model (as typically found for ABs by e.g. Dempsey et al. 1997) with the cluster N_H gives acceptable fits ($\chi^2 = 11.91$ for 9 degrees of freedom). The inferred temperatures of $1.15^{+0.33}_{-0.18}$ and $0.38^{+0.21}_{-0.12} \text{ keV}$, the relative emission measures of the two components (the higher temperature component having $1.4^{+1.6}_{-0.7}$ the emission measure of the cooler), and the inferred luminosity ($L_X(0.5 - 10 \text{ keV}) = 2 - 5 \times 10^{29} \text{ erg s}^{-1}$, at the distance range estimated above) are all consistent with the range of BY Dra systems discussed in Dempsey et al. (1997). We also performed the same fits using unbinned spectra and the C-statistic in XSPEC, finding results that are consistent within the error bars with the results above. Thus, the combined evidence from photometry, proper motion, and the X-ray spectrum strongly indicates that CX8 is a pair of foreground, chromospherically active, M-dwarf binaries, likely of solar or greater abundances.

4.3. Chance Coincidences

In order to estimate the number of chance coincidences of cluster stars with *Chandra* source regions, we computed the number of both MS stars and blue stars expected to fall in each search region. In both cases we considered stars with $R_{625} > 16$. MS stars were defined by $B_{435} - R_{625} \geq 0.6$, while blue stars were defined by $B_{435} - R_{625} < 0.6$. The estimated number of chance coincidences per search area was computed from the radial surface density for each group of stars times the area of the search region. No proper-motion cleaning was applied, since in counting the actual number of objects per search area we did not apply proper-motion cleaning. The predicted number of MS stars per search area was typically within about a factor of two of the observed number, which is consistent given the small-number statistics. On the other hand, the predicted number of blue stars within each search area was minuscule, with a median value of about 0.02. The total number of spurious matches of blue stars with all search areas was predicted to be 0.9. This indicates that the MS stars that are observed within the search areas are almost certainly chance superpositions, while the blue stars are highly likely to be bona fide identifications.

4.4. Comparison with Pooley et al. (2002) and Thomson et al. (2012)

We confirm all of the identifications made by Pooley et al. (2002) except for that of source CX11. Thomson et al. (2012) similarly were unable to confirm this identification. In this case, the situation is complicated by two overlapping diffraction rings around nearby bright stars. While there is a suggestion of extra flux at the location indicated by Pooley et al. (2002), it may simply represent the superposition of the two rings. There are three stars that lie at the edge of the search area, about $0''.3$ from the source position. One of these stars is a subgiant, one is a MSTO star, and the remaining fainter star has an undetermined R_{625} magnitude from KS2. Based on aperture photometry, this star appears likely to lie near the MS. As we discuss in Forestell et al. (2014), source CX11 is within the positional uncertainty of MSP D, which shows no evidence of binarity (Corongiu et al. 2006). Since an isolated neutron star is not expected to have a detectable optical counterpart, it is most likely that the coincidence of the three stars with the source CX11 search area is a chance superposition. In fact, about 1.7 ± 1.3 chance superpositions are expected within the search area for CX11.

Pooley et al. (2002) noted a coincidence between source CX17 and a radio source detected with the Australia Telescope Compact Array. This is consistent with our classification of the CX17 optical counterpart as a galaxy, based on the position of CX17 in the center of a diffuse optical object that clearly seems to be a galaxy (see Fig. 7), interpreting the

radio and X-ray emission as likely both associated with an active galactic nucleus.

We note that Thomson et al. (2012) have suggested a different counterpart to source CX8 than the pair of red stars that we discuss in §4.2 above. They stated that the U and B photometry of their proposed counterpart indicates that it is a “faint gap source,” i.e. that it lies between the MS and the extended blue horizontal branch and thus is a possible CV. However, from the full WFC3 photometry provided by Thomson et al. (2012), it can be seen that their suggested counterpart to CX8 lies on the main sequence in the $(U - B, B)$ CMD (the only filters in which they detected it). Our ACS photometry of this star also indicates that it lies on the MS in both the $(B_{435} - R_{625}, R_{625})$ CMD and the $(H\alpha - R_{625}, R_{625})$ CMD. Thus, based on all the available data, we see no evidence for interpreting it as a CV.

We also note that Thomson et al. (2012) have pointed out that the counterpart proposed by Pooley et al. (2002) for source CX16, which shows the photometric characteristics of a BY Draconis star, is outside of the Pooley et al. (2002) error circle. They suggest another closer star as a more likely counterpart. However, we find that the counterpart proposed by Pooley et al. (2002) is the closest star to the refined source CX16 position from Forestell et al. (2014), falling within the search area at $1.4 r_{\text{err}} = 0''.19$ from the X-ray source location. Thus, we confirm the Pooley et al. (2002) identification of this source.

Thomson et al. (2012) have suggested a possible SX Phoenicis star as a counterpart to source CX12. However, Forestell et al. (2014) were able to resolve CX12 (with the additional *Chandra* data) into three sources (CX20, CX23, and CX24). Consequently, the counterpart suggested by Thomson et al. (2012) lies $0''.75$ from the nearest X-ray position (CX24), well outside our search radius. We suggest counterparts to each of CX20, CX23, and CX24.

4.5. X-ray to Optical Flux Ratios

As in Cohn et al. (2010), we have examined the X-ray to optical flux ratio, f_X/f_{opt} , where we take $f_X(0.5 - 8 \text{ keV})$ from Forestell et al. (2014) and set $f_{\text{opt}} = f_{R_{625}} = 1.07 \times 10^{-(0.4R_{625} + 6)}$. The latter conversion factor is computed from the *HST* flux calibration constants and includes a small correction for the total extinction of $A_R = 0.10 \text{ mag}$. The resulting flux ratio is plotted versus f_X in Fig. 10. The ratio has been observed to be higher for accreting sources, such as CVs and LMXBs, than for ABs (e.g. Edmonds et al. 2003; Bassa et al. 2008).

We have used this observation to support our identification of the counterpart to the source CX5 as a possible CV, on the basis of its high $L_X = 1.1 \times 10^{32} \text{ erg s}^{-1}$ and moderately high $f_X/f_{\text{opt}} = 1.4$. These values are inconsistent with the other objects classified as ABs, with the exception

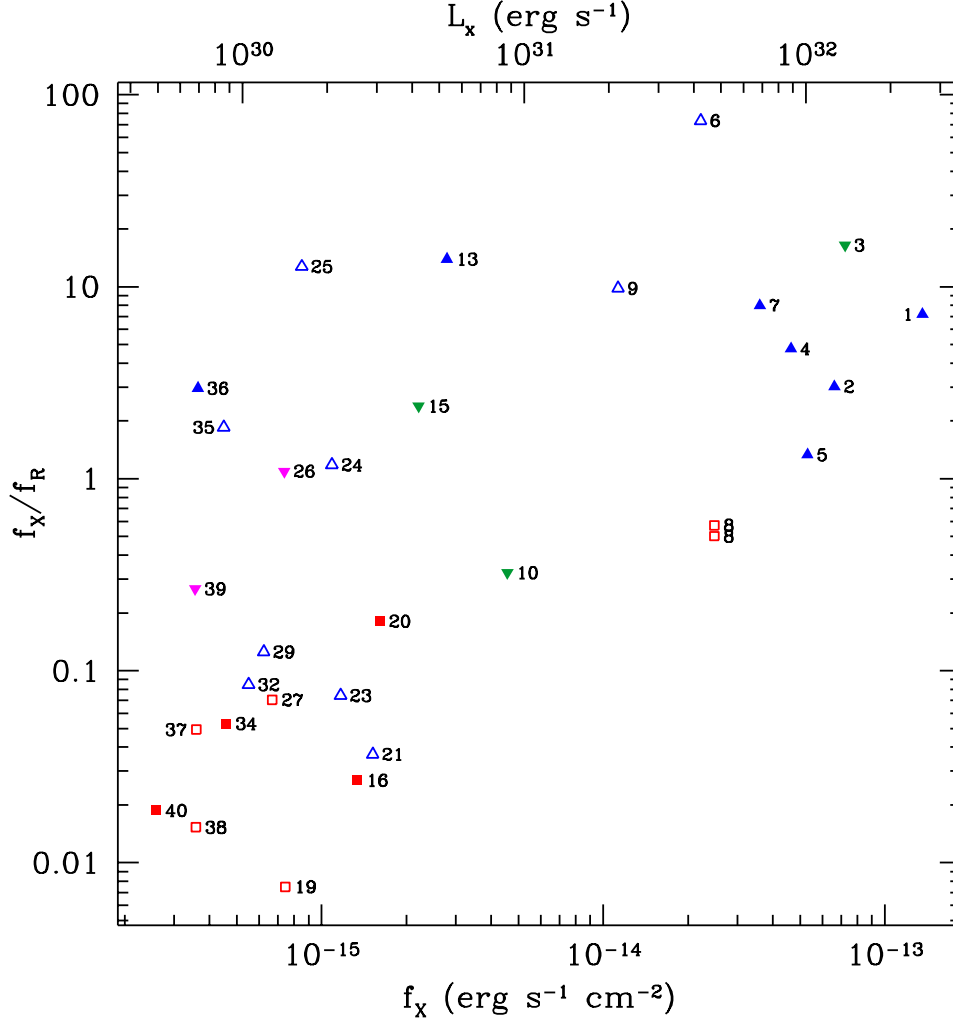


Figure 10. X-ray to optical R_{625} -band flux ratio vs. X-ray flux (0.5–8 keV) for CVs (blue triangles), ABs (red squares), and galaxies (inverted magenta triangles). Less certain identifications are plotted with open symbols. The upper axis gives the equivalent X-ray luminosity assuming that all objects are at the distance of the cluster. Note that the CVs mostly populate the upper part of the diagram, while the ABs mostly populate the lower part.

of CX8. As noted in §4.2, our proposed source CX8 counterpart stands out for its large $H\alpha$ excess, which presumably indicates a high level of chromospheric activity. Its high value of $f_X/f_{\text{opt}} = 0.5$ is consistent with this. As discussed in §4.2, CX8 is likely to be a foreground object, which would significantly reduce its inferred L_X value relative to the cluster members.

It can be seen in Fig. 10 that the objects classified as likely or less certain CVs mostly populate the upper part of the diagram and the likely or less certain AB candidates mostly populate the lower part. The median flux ratio is 60 times larger for the CVs than for the ABs. The two galaxies for which flux ratios were calculated fall in between the bulk of the CVs and the bulk of the ABs. This suggests that they are normal galaxies, rather than active galaxies, for which the flux ratio should be at least an order of magnitude larger.

4.6. Variability

Since our dataset provides a 24-exposure time sequence of $H\alpha$ exposures, with two exposures per orbit, it was possible to investigate optical variability of the detected objects. The time sequence samples time scales shorter than about one hour (the visibility period per *HST* orbit) and also time scales of days to months. As a measure of the variability, we first adopted the 3σ -clipped RMS deviation, which we used in our study of NGC 6397 (Cohn et al. 2010).⁵ Since the use of sigma clipping rejects outliers, this approach results in a measure of variability that is most sensitive to the orbital variability of binary systems, rather than large-amplitude fluctuations of CVs.

⁵ Following a suggestion of the referee, we now compute the fractional RMS deviation of the fluxes and express this in magnitude units.

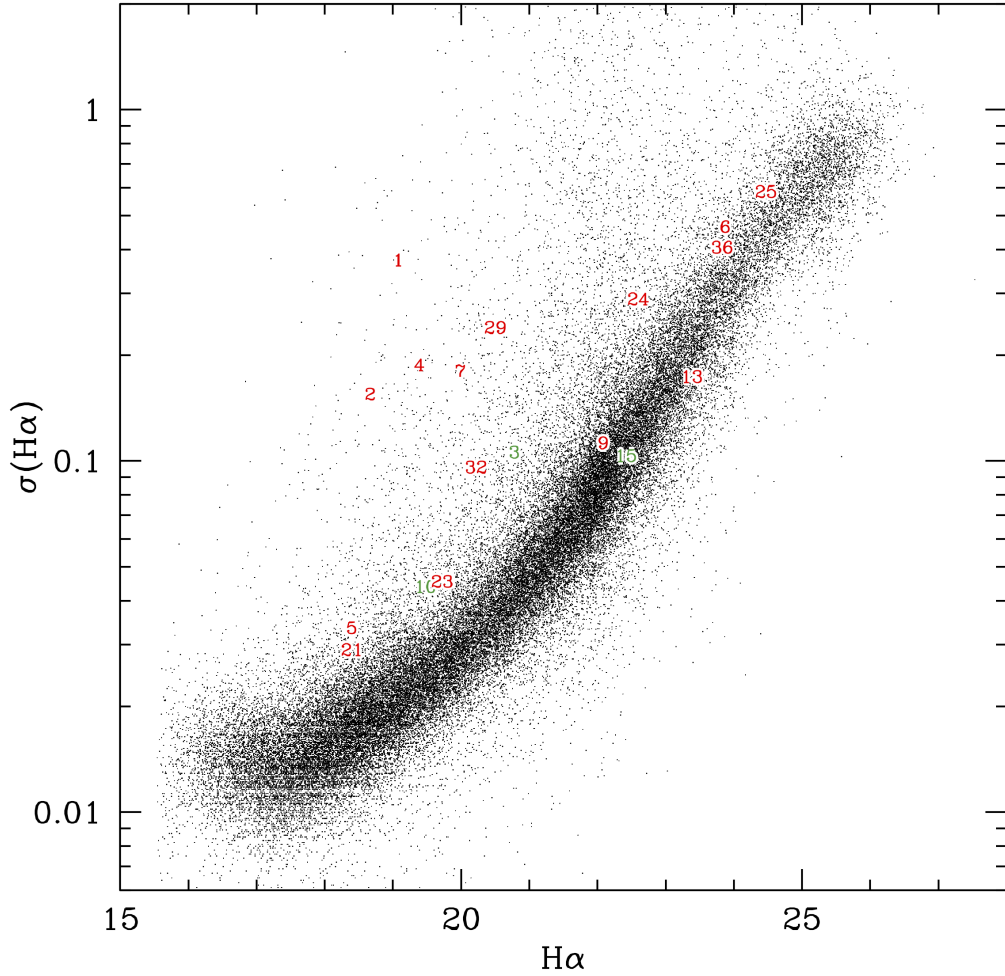


Figure 11. $H\alpha$ variability versus $H\alpha$ magnitude for candidate CVs. The ordinate is the 3σ -clipped RMS deviation of the up to 24 $H\alpha$ measurements for each star. The locations of the CV candidates are plotted as numbers over the distribution for all stars. Note that most of the bright CVs show a variability signal, i.e. they lie above the relation defined by the majority of the stars.

We plot $\sigma(H\alpha)$ versus mean $H\alpha$ magnitude in Figs. 11 and 12. It can be seen in these figures that most stars fall along a “fundamental” sequence of increasing $\sigma(H\alpha)$ with increasing magnitude. We interpret stars falling above this sequence as showing evidence of optical variability, although some degree of photometric scatter is also clearly present. We have plotted the locations of the *Chandra* source counterparts on this diagram. A number of the counterparts show apparently significant variability. This group includes many of the bright CV counterparts, viz. sources CX1, CX2, CX4, CX7, CX29, and CX32 as seen in Fig. 11. Four of the remaining bright CV candidate counterparts, sources CX5, CX21, and CX23, show marginal evidence of variability, falling just above the fundamental sequence. Of the faint CV candidate counterparts, sources CX6 and CX24 show marginal evidence of variability and sources CX9, CX13, and CX36 fall on the high side of the fundamental sequence. At the magnitude

of these faint CVs, $H\alpha \approx 24$, the large typical photometric uncertainty of about 0.3 mag makes it difficult to detect moderate variability. The amplitude of the variability measured by $\sigma(H\alpha)$ for the bright CVs is about 0.1 – 0.3 mag, which is typical for orbital variations. The variability plot for the ABs is shown in Fig. 12. It can be seen from this figure that sources CX8, CX19, and CX27 show evidence of variability. As discussed in §4.2, source CX8 appears to be a foreground system.

We also investigated the total range of the $H\alpha$ magnitudes for each object in order to search for outburst behavior in the CV counterparts. In order to filter out cosmic-ray events that affect some of the individual magnitude measurements, we chose the fainter of the magnitude measurements from each of the pair of $H\alpha$ frames per orbit. We discarded orbits for which there was only one successful $H\alpha$ magnitude measurement. We plot the total range of the orbital $H\alpha$ magnitudes

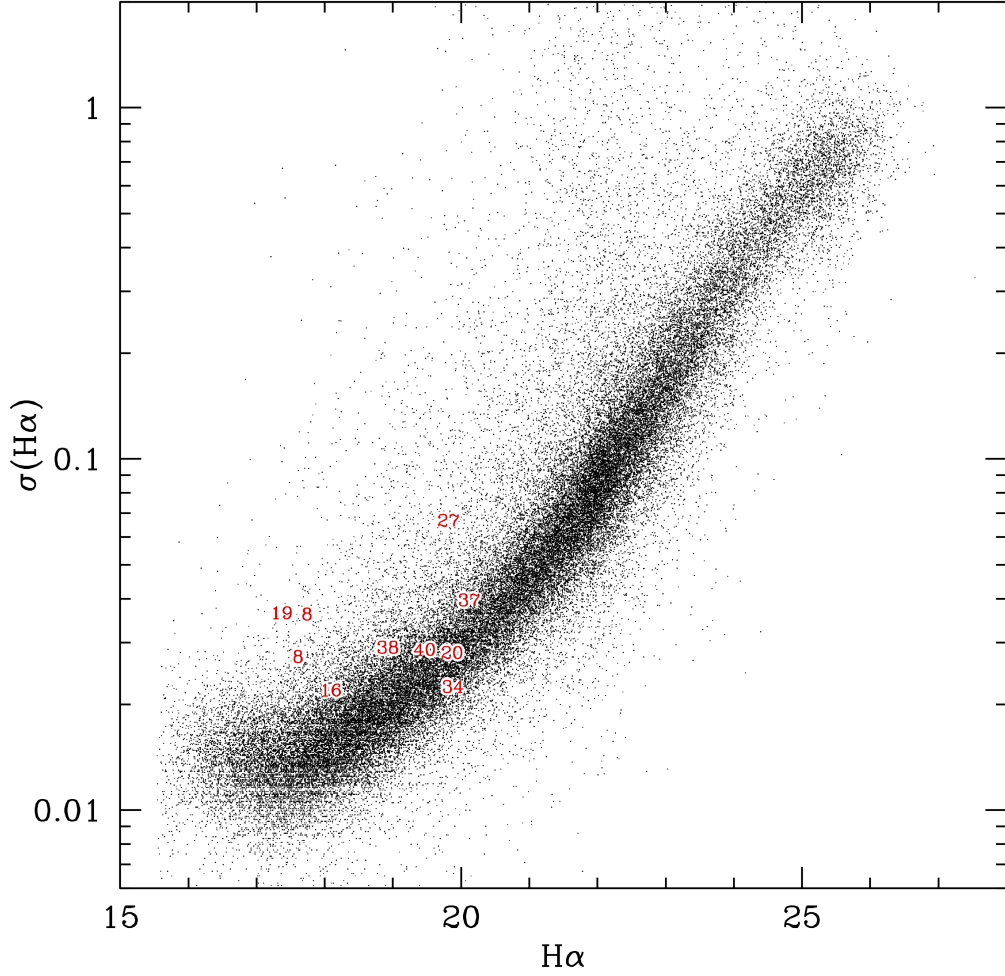


Figure 12. $H\alpha$ variability versus $H\alpha$ magnitude for candidate ABs. Note that the ABs, on average, show lower variability than the CVs illustrated in Fig. 11.

versus $H\alpha$ magnitude for all the stars, with the CV counterparts indicated, in Fig. 13. Five of the bright CV counterparts have a variation range of $\sim 0.5 - 1.0$ mag. The source CX1 stands out with the largest range of $H\alpha$, with a value of ~ 1.3 mag. While some of this variation range may be due to photometric uncertainty, examination of the individual images indicates that it is largely due to actual flux variation. Thus, source CX1 appears to have undergone a dwarf nova outburst during the approximately 180 d interval over which the data were obtained. We note that Kaluzny & Thompson (2009) observed a 1.5 mag amplitude outburst from the CX4 counterpart, in a study of stellar variability in NGC 6752 that included the locations of all of the Pooley et al. (2002) *Chandra* sources. Thomson et al. (2012) observed an outburst of 1.5 mag amplitude from the CX1 counterpart and an outburst of 6 mag amplitude from the CX7 counterpart.

Kaluzny & Thompson (2009) detected periodic variability from a suggested counterpart to CX19. They found a period

of 0.11306 d, with an amplitude of a few hundredths of a mag. They note that if this modulation is due to ellipsoidal variations, then the orbital period would be twice this large, viz. 0.226 d. While we were not able to confirm the periodicity of this counterpart with a period-folding analysis of the $H\alpha$ time series, Fig. 12 indicates that the object is variable, with an amplitude of about 0.04 mag. We note that Thomson et al. (2012) did not find any evidence of the Kaluzny & Thompson (2009) periodicity in their WFC3 near-UV data. Kaluzny & Thompson (2009) suggest that the counterpart to CX19 is a close binary hosting a neutron star or a black hole. However, its location to the red of the MS in the $(B_{435} - R_{625}, R_{625})$ CMD and its low X-ray to optical flux ratio of $f_X/f_{\text{opt}} = 0.007$ suggest instead that it is likely to be an AB. In this case, the longer orbital period of 0.226 d is strongly preferred, since even the contact binaries in 47 Tuc in this range of stellar masses have periods of at least 0.20 d (Albrow et al. 2001).

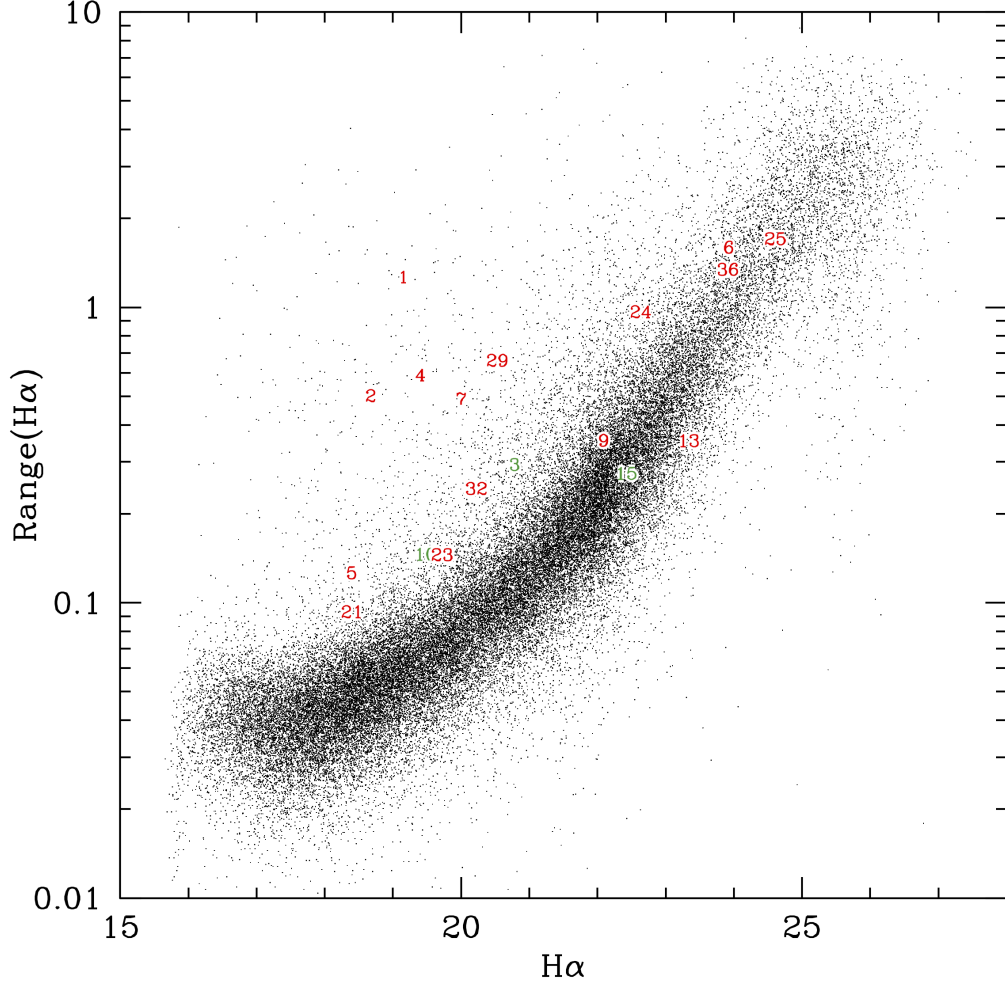


Figure 13. $H\alpha$ range versus $H\alpha$ magnitude for candidate CVs. The ordinate is the full range of the up to 12 $H\alpha$ measurements for each star, as we took the faintest of each pair of $H\alpha$ measurements as representing the best estimate of the $H\alpha$ magnitude for that orbit. The CV candidates are plotted as numbers over the distribution for all stars. Note the similarity between this figure and Fig. 11, other than the greater amplitude of the variability here.

4.7. Spatial Distribution

We determined the cluster center by iterative centroiding in a $12''$ radius aperture using a sample of stars with magnitudes in the range $R_{625} < 20.5$, which extends to 4 mag below the MSTO. The resulting center of $\alpha = 19^{\text{h}} 10^{\text{m}} 52^{\text{s}}.12$, $\delta = -59^{\circ} 59' 4''.4$ agrees well with the recent center determinations by Goldsbury et al. (2010) and Thomson et al. (2012), differing from the former by $0''.11$ and from the latter by $0''.15$. Experimentation with the centroiding aperture size and the stellar sample definition indicates that the center position is uncertain by about $0''.5$.

We next determined both the cumulative radial distribution and a binned radial profile for a MSTO group of stars with magnitudes in the range $16 \leq R_{625} < 18.5$, which extends to 2 mag below the MSTO. These are shown in Fig. 14. In order to assess the overall behavior of the cluster profile, we

fitted the cumulative radial distribution of the MSTO group with a “generalized King model,” which we have also called a “cored power law.” As discussed by Cohn et al. (2010), this takes the form

$$S(r) = S_0 \left[1 + \left(\frac{r}{r_0} \right)^2 \right]^{\alpha/2}, \quad (1)$$

with the core radius r_c related to the scale parameter r_0 by,

$$r_c = \left(2^{-2/\alpha} - 1 \right)^{1/2} r_0. \quad (2)$$

Fig. 14 shows the resulting maximum-likelihood fit where the data have been fitted to a limiting radius of $r_h = 115''$. As seen in Fig. 1, the region within r_h is fully covered by the ACS/WFC imaging. While the model provides a statistically acceptable fit to the profile over this data range, it can

be seen in the right panel of Fig. 14 that the fit is systematically low in the central region of the cluster and high in an intermediate radial range. Moreover, the best-fit slope of $\alpha = -1.28$ also does not agree with that expected for an “analytic King model,” for which $\alpha = -2$. Thus, the radial profile of NGC 6752 is not well fitted by a single-mass King model, indicating that it does not have a normal-core structure like clusters such as 47 Tuc (Howell et al. 2000). This suggests that NGC 6752 is in a post-collapse state of evolution as concluded by several previous studies noted above (Djorgovski & King 1986; Ferraro et al. 2003; Thomson et al. 2012). In order to evaluate the parameters of the expected post-collapse surface-density cusp, we fitted the cored-power-law model (Eqn. 1) to the cumulative radial distribution using an outer limiting radius of $25''.8$, corresponding to a radial scale of 0.5 pc, which is the limiting radius adopted by Lugger et al. (1995) for the cored-power-law fits they presented for 15 candidate core-collapsed clusters. The fits are shown in Fig. 15. The best-fit parameter values are $r_c = 4.6'' \pm 1.5''$ and $\alpha = -0.82 \pm 0.07$. These indicate that NGC 6752 has a well-resolved core, with a surrounding cusp slope that agrees well with the mean core-collapse slope of -0.84 ± 0.10 found by Lugger et al. (1995). We note that they similarly found that a cored power law gave a good fit to the central U -band surface-brightness profile of NGC 6752 with best-fit parameters of $r_c = 6.7'' \pm 1.9''$ and $\alpha = -0.97 \pm 0.15$. These two sets of best-fit parameter values are consistent with each other to within 1σ . In retrospect, we conclude that our “conservative” interpretation, in Lugger et al. (1995), that NGC 6752 is not required to be in a post-collapse state, is too conservative and that the surface-density profile of NGC 6752 provides good evidence that the cluster has indeed experienced core collapse.

We next examined the radial profiles of a number of different stellar groups by comparing the cumulative radial distributions shown in Fig. 16. The particular groups considered are the MSTO group described above, all of the 39 *Chandra* sources within r_h , the nine brightest CVs, the five faintest CVs, the ABs, and a blue straggler (BS) group selected from the CMD as illustrated in Fig. 17. As can be seen in Fig. 16, the *Chandra* sources, the bright CVs, and the BSs show strong central concentration relative to the MSTO group. In order to quantify the significance of the differences in the distributions, we performed Kolmogorov-Smirnov (K-S) comparisons of each sample with the MSTO group. The results are given in Table 2, where the probability, p , of the two samples being drawn from the same parent distribution is listed. The distributions of the *Chandra* sources, the bright CVs, and the BSs differ very significantly ($p < 1\%$) from that of the MSTO group. The faint CV and AB distributions do not differ from the MSTO group at a significant level ($p = 31\%$ and $p = 27\%$, respectively). A direct comparison

of the bright and faint CVs indicates that these two groups differ at the 6% level. While this misses a 5% cutoff for statistical significance, it clearly suggests a meaningful difference between the two distributions.

In order to further investigate the spatial distribution of the various *Chandra* sources and BSs in NGC 6752, we carried out maximum-likelihood fits of the cored-power-law model to the surface-density distributions of the groups shown in Fig. 16. As discussed by Cohn et al. (2010), this procedure provides an estimate for the characteristic mass of an object in each group relative to the MSTO mass. As in Cohn et al. (2010), we adopt the approximation that the mass groups above the MSTO mass are in thermal equilibrium. In this case, the surface-density profile for a mass group with mass m is given by Eqn. 1 with a slope parameter α related to the turnoff-mass slope α_{to} by

$$\alpha = q(\alpha_{to} - 1) + 1 \quad (3)$$

where $q = m/m_{to}$.

Table 2 gives the results of maximum-likelihood fits of Eqn. 1 to the turnoff-mass stars, *Chandra* sources, CVs, ABs, and BSs. As can be seen from the table, the q values for all of the groups exceed unity, indicating that the characteristic masses exceed the turnoff mass. We assume a MSTO mass of $0.80 \pm 0.05 M_\odot$, based on the study of Gruyters et al. (2014), who found a MSTO mass of $0.79 M_\odot$. For the *Chandra* sources, bright CVs, and BSs, the excesses are significant at the $2.4\sigma - 3.2\sigma$ level. We note that the results of this analysis are supported by the K-S comparison results given in the last column of the table.

The inferred mass range for the bright CVs ($1.6 \pm 0.3 M_\odot$) is similar to what we found for NGC 6397. The median R_{625} -band absolute magnitude for these systems is about $M_R \approx 7$. Assuming that the R_{625} -band flux is dominated by the secondary, this implies a secondary mass of about $0.6 M_\odot$, based on the isochrones of Baraffe et al. (1997). The corresponding WD mass is $M_{WD} \sim 1.0 M_\odot$, which is consistent with the value of $0.83 \pm 0.23 M_\odot$ found by Zorotovic et al. (2011). The inferred mass range for the faint CVs ($1.0 \pm 0.2 M_\odot$) is consistent with a somewhat lower mass white dwarf (e.g. $M_{WD} \sim 0.8 M_\odot$) and a secondary mass that has been whittled down to $\lesssim 0.2 M_\odot$. In such a system, the optical flux would be dominated by the white dwarf, as observed here.

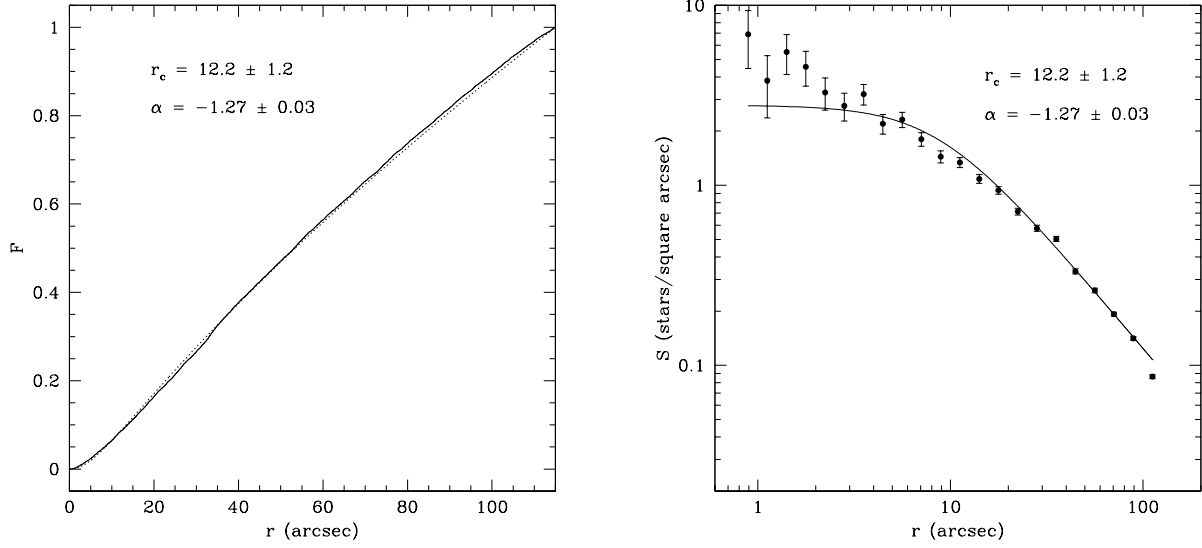


Figure 14. Radial surface-density profile for the MSTO group. Left panel: cumulative radial distribution (solid line) with a cored-power-law fit to 115'' (dashed line). Right panel: binned surface-density profile with the same cored-power-law fit. A one-sample K-S test indicates that the data are consistent with the fit with a probability of 14%. Nevertheless, the curve falls systematically below the data for $r < 5''$ and above the data for $5'' < r < 20''$.

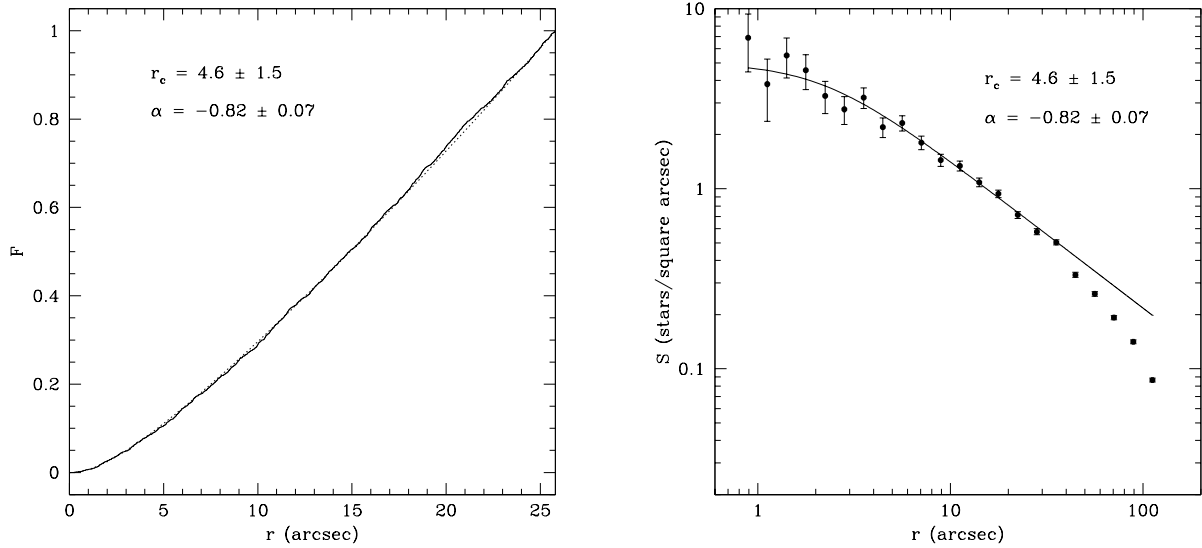


Figure 15. Radial surface-density profile for the MSTO group as in Fig. 14. Left panel: cumulative radial distribution (solid line) with a cored-power-law fit to $25''/8 = 0.5$ pc (dashed line). Right panel: binned surface-density profile with the same cored-power-law fit. Note that the fit to the inner profile is much better than that shown in Fig. 14.

5. DISCUSSION

As in NGC 6397, the bright CVs have a more centrally concentrated distribution than the faint CVs. As we discussed for that cluster, this is consistent with the bright CVs representing a recently formed population that is produced by dynamical interactions near the cluster center. These interactions may likely include exchange interactions in which a heavy white dwarf displaces a member of a primordial binary. As these CVs age, the secondary loses mass and the

accretion rate drops, leading to a reduction in both the optical and X-ray luminosity (Howell et al. 2001). At the same time, two-body interactions with singles and other binaries scatter the CVs into larger orbits that put them at increasing distance from the cluster center.

We note that Hong et al. (2017) have recently reported Monte-Carlo simulations of globular cluster dynamical evolution that include CV formation from primordial binaries and subsequent evolution. They find that the CVs are more

Table 2. Cored-power-law Model Fits to 115''

Sample	N^a	q	$r_c (")$	α	$m (M_\odot)$	σ^b	K-S prob ^c
MSTO	10016	1.0	12.2 ± 1.2	-1.27 ± 0.03	0.80 ± 0.05
<i>Chandra</i> sources	39	1.33 ± 0.12	8.5 ± 0.8	-2.07 ± 0.28	1.06 ± 0.10	2.4	0.080%
bright CV	9	2.03 ± 0.35	6.0 ± 0.8	-3.60 ± 0.79	1.62 ± 0.28	2.9	0.042%
faint CV	5	1.27 ± 0.24	9.0 ± 2.0	-1.88 ± 0.54	1.02 ± 0.19	1.1	31%
AB	9	1.31 ± 0.24	8.8 ± 1.8	-1.97 ± 0.54	1.05 ± 0.19	1.3	27%
BS	30	1.41 ± 0.11	8.1 ± 0.7	-2.21 ± 0.26	1.13 ± 0.09	3.2	0.54%

^aSize of sample within 115'' of cluster center

^bSignificance of mass excess above MSTO mass

^cK-S probability of consistency with MSTO group

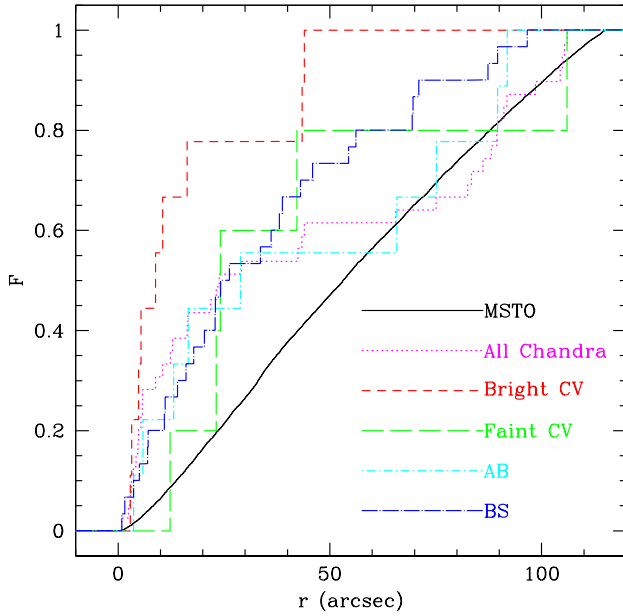


Figure 16. Cumulative radial distributions for selected stellar groups. Note that the *Chandra* sources, the bright CVs, and the BSs show significant central concentration ($p \lesssim 1\%$) relative to the MSTO group. Fitting information and K-S sample comparisons for these stellar groups are given in Table 2.

centrally concentrated than the MSTO-mass stars, with the effect being stronger for the CVs that form from primordial binaries that have undergone an exchange encounter. This exchange group includes a population of CVs that are more massive than those formed from primordial binaries that have not undergone an exchange encounter. The resulting greater central concentration of the more massive CVs is qualitatively consistent with our inference that the brighter CVs in NGC 6752 are more massive than the fainter ones. [Hong](#)

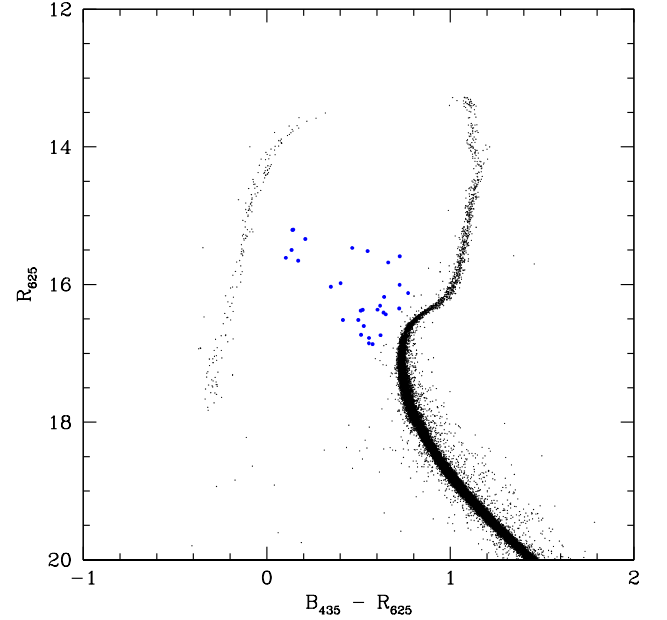


Figure 17. Color-magnitude diagram showing the selection of blue stragglers for the radial distribution analysis. A conservative selection criterion was used to choose 30 BS candidates within the half-mass radius.

[et al. \(2017\)](#) note that the radial distribution of the CVs reflects, “the remaining memory of the CV formation history and progenitor masses,” as well as the present CV mass. Thus, our estimate of CV masses based on the assumption that they have achieved their equilibrium radial distribution should be viewed as a first approximation to a complex process.

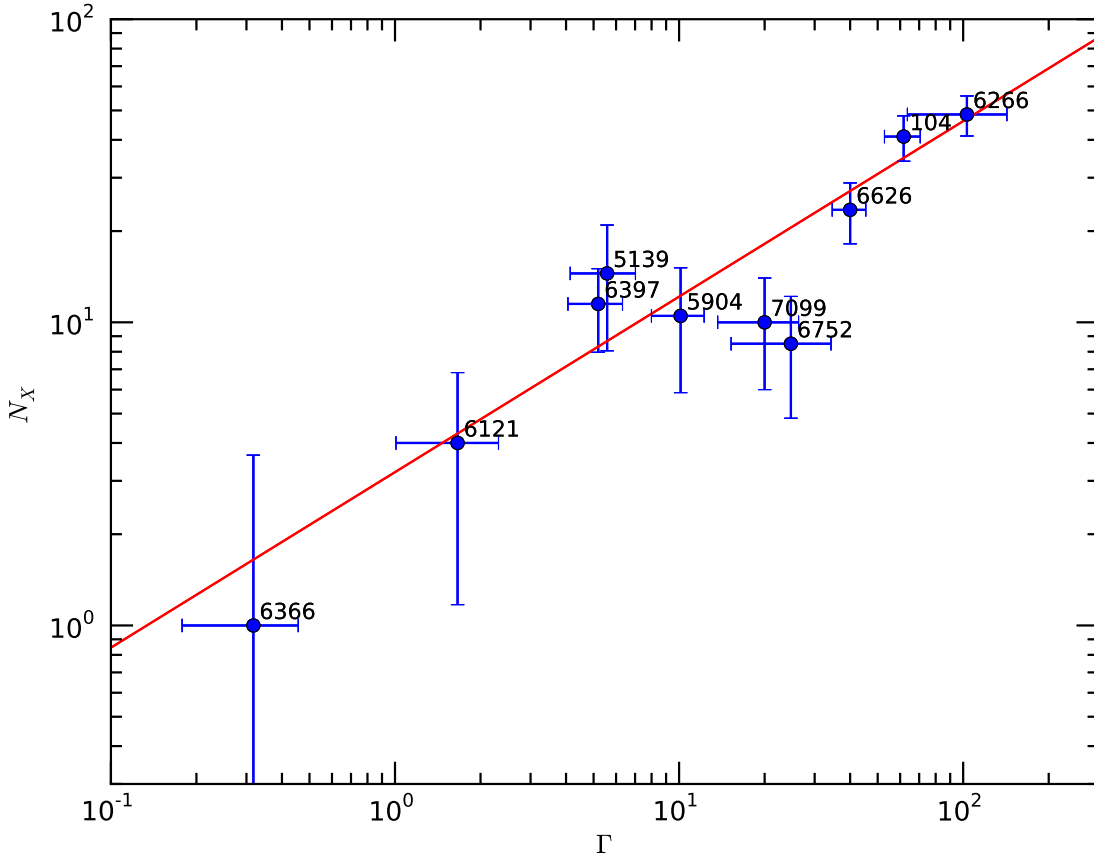


Figure 18. Number of X-ray sources versus the stellar encounter rate Γ based on data from Bahramian et al. (2013). The red line shows a linear regression in log-log space, corresponding to the relation $N_X \propto \Gamma^{0.58 \pm 0.10}$.

5.1. Stellar Encounter Rate

Bahramian et al. (2013) have reexamined the relationship between the number of X-ray sources in a cluster and the stellar encounter rate that was originally found by Pooley et al. (2003). Fig. 18 shows the Bahramian et al. (2013) dataset. The errors in the encounter rate Γ are adopted from their study, while the errors in the background-corrected source counts include the Poisson errors in both the total source counts and the background counts. The line in Fig. 18 is a linear regression that corresponds to the relation $N_X \propto \Gamma^{0.58 \pm 0.10}$. The slope value is consistent with the value of 0.74 ± 0.36 obtained by Pooley et al. (2003). It can be seen from Fig. 18 that the core-collapsed clusters NGC 6752 and NGC 7099 both fall below the mean relation defined by the entire cluster sample. NGC 6752 is 3.0σ below the relation, while NGC 7099 is 2.0σ below. In contrast, Pooley et al. (2003) found that the core-collapsed cluster NGC 6397 lies above the relation. This deviation of NGC 6397 from the relation is not statistically significant in our analysis. Our linear regression analysis quantifies the suggestion of Bahramian

et al. (2013) that core-collapsed clusters underproduce X-ray binaries relative to their computed encounter rates. This may indicate that binary destruction/ejection is a more vigorous process in core-collapsed clusters than in those that are in a pre-collapse state.

Ivanova et al. (2006) found, from their Monte-Carlo simulations of CV formation and evolution in globular cluster environments, that clusters that underwent core collapse in the past 1 – 2 Gyr will have a depleted number of CVs, since CVs that have been destroyed during core collapse will not yet have been replaced by newly formed CVs. However, the recent Monte-Carlo simulations of CV evolution in dynamically evolving clusters by Belloni et al. (2017) do not show such a clear effect.

6. SUMMARY

We have searched for optical counterparts to the 39 *Chandra* sources that lie within the half-mass radius of NGC 6752, using *HST* ACS/WFC imaging in B_{435} , R_{625} , and $H\alpha$. Based primarily on CMD classification, we found plausible counterparts to 31 of the sources. These include 16 likely

or less certain CVs, nine likely or less certain ABs, three galaxies, and three more likely than not AGNs. Our CV/AB discrimination that is based on CMD location is generally supported by the X-ray to optical flux ratios for these identifications. The CVs have, in most cases, significantly higher values of f_X/f_{opt} than do the ABs, as expected.

In comparison to our results for NGC 6397, where all of the CV candidates exhibited a strong $H\alpha$ excess in the ($H\alpha - R_{625}$, R_{625}) CMD (Cohn et al. 2010), many of the CV candidates reported here do not. We examined the color-color diagram to further investigate this issue and found that all but three of our CV candidates do show a $H\alpha$ excess relative to other stars of the same $B_{435} - R_{625}$ color. However, it is not clear why the $H\alpha$ excesses of the CV candidates in NGC 6752 are generally weaker than those of the CV candidates in NGC 6397.

As expected, most of the bright CV candidates registered significant time variability. The amplitude of the variability, as measured by the 3σ -clipped RMS of the $H\alpha$ time series, is typically $\sim 0.1 - 0.3$ mag, which is characteristic of orbital variations. The counterpart to source CX1 showed a ~ 1.3 mag total range of variability, which is consistent with a dwarf nova eruption. The ABs showed substantially less evidence of variability, with only the counterparts to CX8, CX19, and CX27 falling significantly above the $\sigma(H\alpha)$ - $H\alpha$ relation for all stars. Of these three, the two counterparts to CX8 appear to be a foreground objects that are not associated with the cluster.

Our determination of the cluster center agreed well with previous recent determinations. We found that while the radial profile of a MSTO star group can be acceptably fitted with a cored power law out to the half-mass radius, this model falls systematically below the profile in the core and above it at intermediate radii. In addition, the slope for this cored-power-law fit does not agree with that of an analytic King model. Thus, we conclude that NGC 6752 does not show a normal King model profile, in agreement with the previous findings of Djorgovski & King (1986), Ferraro et al. (2003), and Thomson et al. (2012). The profile is better fit,

out to a projected radius of 0.5 pc, by a cored power law with a slope that is consistent with the typical value for a post-core-collapse profile. This supports the conclusion that NGC 6752 is in a post-collapse state.

We compared the radial distributions of several different stellar groups to that of a MSTO sample. We found that radial distributions of all of the *Chandra* sources, the bright CVs, and the BSs show a strongly significant central concentration relative to that of the MSTO group. We performed fits of a cored-power-law model to the individual groups, in order to estimate the characteristic individual stellar mass for each group. We found that the *Chandra* sources, the bright CVs, and the BSs all have a characteristic mass that significantly exceeds the MSTO mass. In the case of the bright CVs, the characteristic mass of $1.6 \pm 0.3 M_{\odot}$ is the similar to what we found for NGC 6397 (Cohn et al. 2010).

We found that the bright CVs are more centrally concentrated than the faint CVs, consistent with a picture in which bright CVs represent a population that has been recently formed by dynamical interactions near the cluster center. The faint CVs then would represent an evolved population that has been scattered out of the cluster core over time. We find that, like the core-collapsed cluster NGC 7099, NGC 6752 is deficient in X-ray sources relative to the mean relation between X-ray source population size and encounter rate. This supports the suggestion that core-collapsed clusters underproduce X-ray binaries, implying that binary destruction/ejection is more vigorous in core-collapsed clusters.

We thank N. Ivanova for providing unpublished details on her simulations of CVs in globular clusters. This work is supported by NASA grant HST-GO-12254.02-A to Indiana University. Phyllis Lugger and Haldan Cohn acknowledge the hospitality of the Department of Astronomy and Astrophysics at the University of California Santa Cruz, where part of this work was carried out. Craig Heinke is supported by a NSERC Discovery Grant and a NSERC Discovery Accelerator Supplement Award.

Software: IRAF, PyRAF, SExtractor, wavdetect, pwdetect, XSPEC

REFERENCES

- Albrow, M. D., Gilliland, R. L., Brown, T. M., et al. 2001, *ApJ*, 559, 1060
- Anderson, J., Sarajedini, A., Bedin, L. R., et al. 2008, *AJ*, 135, 2055
- Annunziatella, M., Mercurio, A., Brescia, M., Cavuoti, S., & Longo, G. 2013, *PASP*, 125, 68
- Bahramian, A., Heinke, C. O., Sivakoff, G. R., & Gladstone, J. C. 2013, *ApJ*, 766, 136
- Baraffe, I., Chabrier, G., Allard, F., & Hauschildt, P. H. 1997, *A&A*, 327, 1054
- Bassa, C. G., Pooley, D., Verbunt, F., et al. 2008, *A&A*, 488, 921
- Beccari, G., De Marchi, G., Panagia, N., & Pasquini, L. 2014, *MNRAS*, 437, 2621
- Belloni, D., Giersz, M., Rocha-Pinto, H. J., Leigh, N. W. C., & Askar, A. 2017, *MNRAS*, 464, 4077
- Bertin, E., & Arnouts, S. 1996, *A&AS*, 117, 393

- Binney, J., & Merrifield, M. 1998, *Galactic Astronomy* (Princeton, NJ: Princeton Univ. Press)
- Bogdanov, S., van den Berg, M., Heinke, C. O., et al. 2010, *ApJ*, 709, 241
- Bogdanov, S., van den Berg, M., Servillat, M., et al. 2011, *ApJ*, 730, 81
- Castelli, F., & Kurucz, R. L. 2004, *ArXiv Astrophysics e-prints*, astro-ph/0405087
- Cohn, H. N., Lugger, P. M., Couch, S. M., et al. 2010, *ApJ*, 722, 20
- Cool, A. M., Haggard, D., Arias, T., et al. 2013, *ApJ*, 763, 126
- Corongiu, A., Possenti, A., Lyne, A. G., et al. 2006, *ApJ*, 653, 1417
- Dempsey, R. C., Linsky, J. L., Fleming, T. A., & Schmitt, J. H. M. M. 1997, *ApJ*, 478, 358
- Djorgovski, S., & King, I. R. 1986, *ApJL*, 305, L61
- Edmonds, P. D., Gilliland, R. L., Heinke, C. O., & Grindlay, J. E. 2003, *ApJ*, 596, 1197
- Ferraro, F. R., Possenti, A., Sabbi, E., et al. 2003, *ApJ*, 595, 179
- Forestell, L. M., Heinke, C. O., Cohn, H. N., et al. 2014, *MNRAS*, 441, 757
- Gänsicke, B. T., Dillon, M., Southworth, J., et al. 2009, *MNRAS*, 397, 2170
- Gentile, P. A., Roberts, M. S. E., McLaughlin, M. A., et al. 2014, *ApJ*, 783, 69
- Goldsbury, R., Richer, H. B., Anderson, J., et al. 2010, *AJ*, 140, 1830
- Gruyters, P., Nordlander, T., & Korn, A. J. 2014, *A&A*, 567, A72
- Harris, W. E. 1996, *AJ*, 112, 1487
- Heinke, C. O. 2010, in *International Conference on Binaries*, AIP Conf. Ser. 1314, ed. V. Kologera & M. van der Sluys (Melville, NY: AIP), 135
- Heinke, C. O., Grindlay, J. E., Lugger, P. M., et al. 2003, *ApJ*, 598, 501
- Heinke, C. O., Rybicki, G. B., Narayan, R., & Grindlay, J. E. 2006, *ApJ*, 644, 1090
- Hernandez, C., Cool, A. M., Anderson, J., et al. 2013, in *American Astronomical Society Meeting Abstracts*, Vol. 221, American Astronomical Society Meeting Abstracts, #250.41
- Hong, J., van den Berg, M., Schlegel, E. M., et al. 2005, *ApJ*, 635, 907
- Hong, J., Vesperini, E., Belloni, D., & Giersz, M. 2017, *MNRAS*, 464, 2511
- Howell, J. H., Guhathakurta, P., & Gilliland, R. L. 2000, *PASP*, 112, 1200
- Howell, S. B., Nelson, L. A., & Rappaport, S. 2001, *ApJ*, 550, 897
- Ivanova, N., Heinke, C. O., Rasio, F. A., et al. 2006, *MNRAS*, 372, 1043
- Kafka, S., & Honeycutt, R. K. 2006, *AJ*, 132, 1517
- Kaluzny, J., & Thompson, I. B. 2009, *AcA*, 59, 273
- Liedahl, D. A., Osterheld, A. L., & Goldstein, W. H. 1995, *ApJL*, 438, L115
- Lugger, P. M., Cohn, H. N., & Grindlay, J. E. 1995, *ApJ*, 439, 191
- Pooley, D., & Hut, P. 2006, *ApJL*, 646, L143
- Pooley, D., Lewin, W. H. G., Homer, L., et al. 2002, *ApJ*, 569, 405
- Pooley, D., Lewin, W. H. G., Anderson, S. F., et al. 2003, *ApJL*, 591, L131
- Sirianni, M., Jee, M. J., Benítez, N., et al. 2005, *PASP*, 117, 1049
- Taylor, J. M., Grindlay, J. E., Edmonds, P. D., & Cool, A. M. 2001, *ApJL*, 553, L169
- Thomson, G. S., Knigge, C., Dieball, A., et al. 2012, *MNRAS*, 423, 2901
- Verbunt, F., & Lewin, W. H. G. 2006, in *Compact Stellar X-ray Sources*, ed. W. H. G. Lewin & M. van der Klis (Cambridge, UK: Cambridge Univ. Press), 341
- Zorotovic, M., Schreiber, M. R., & Gänsicke, B. T. 2011, *A&A*, 536, A42
- Zurek, D. R., Knigge, C., Maccarone, T. J., et al. 2016, *MNRAS*, 460, 3660